ARO 25045.31-EL

②

MICROWAVE LABORATORY REPORT NO. 89-P-4

PLANAR INTEGRATED CIRCUITS FOR MICROWAVE
TRANSMISSION AND RECEPTION

AD-A217 676

TECHNICAL REPORT

JOEL BIRKELAND AND TATSUO ITOH

DTIC
ELECTE
S JAN24 1990
B D

AUGUST 1989

UNITED STATES ARMY RESEARCH OFFICE
CONTRACT NUMBER DAAL03-88-K-005

TEXAS ADVANCED TECHNOLOGY PROGRAM

THE UNIVERSITY OF TEXAS AT AUSTIN
DEPARTMENT OF ELECTRICAL AND COMPUTER
ENGINEERING
AUSTIN TEXAS 78712

90 01 23 015

MICROWAVE LABORATORY REPORT NO. 89-P-4

PLANAR INTEGRATED CIRCUITS FOR MICROWAVE
TRANSMISSION AND RECEPTION

TECHNICAL REPORT

JOEL BIRKELAND AND TATSUO ITOH

AUGUST 1989

THE UNIVERSITY OF TEXAS AT AUSTIN
DEPARTMENT OF ELECTRICAL AND COMPUTER
ENGINEERING
AUSTIN TEXAS 78712

REPORT DOCUMENTATION PAGE

1a. REPORT SECURITY CLASSIFICATION	1b. RESTRICTIVE MARKINGS
Unclassified	

2a. SECURITY CLASSIFICATION AUTHORITY	3. DISTRIBUTION / AVAILABILITY OF REPORT
2b. DECLASSIFICATION / DOWNGRADING SCHEDULE	Approved for public release; distribution unlimited.

4. PERFORMING ORGANIZATION REPORT NUMBER(S)	5. MONITORING ORGANIZATION REPORT NUMBER(S)
Microwave Laboratory Report No. 89-P-4	ARO 25045.31-EL

6a. NAME OF PERFORMING ORGANIZATION	6b. OFFICE SYMBOL (If applicable)	7a. NAME OF MONITORING ORGANIZATION
The University of Texas Dept. of Elec. & Comp. Eng.		U. S. Army Research Office

6c. ADDRESS (City, State, and ZIP Code)	7b. ADDRESS (City, State, and ZIP Code)
24th & Speedway, ENS 634 Austin, Texas 78712	P. O. Box 12211 Research Triangle Park, NC 27709-2211

8a. NAME OF FUNDING / SPONSORING ORGANIZATION	8b. OFFICE SYMBOL (If applicable)	9. PROCUREMENT INSTRUMENT IDENTIFICATION NUMBER
U. S. Army Research Office		DAAL03-88-K-0005

8c. ADDRESS (City, State, and ZIP Code)	10. SOURCE OF FUNDING NUMBERS			
P. O. Box 12211 Research Triangle Park, NC 27709-2211	PROGRAM ELEMENT NO.	PROJECT NO.	TASK NO.	WORK UNIT ACCESSION NO.

11. TITLE (Include Security Classification)

Planar Integrated Circuits for Microwave Transmission and Reception

12. PERSONAL AUTHOR(S)
Joel Birkeland and Tatsuo Itoh

13a. TYPE OF REPORT	13b. TIME COVERED		14. DATE OF REPORT (Year, Month, Day)	15. PAGE COUNT
Technical	FROM _____	TO _____	August 1989	109

16. SUPPLEMENTARY NOTATION The view, opinions and/or findings contained in this report are those of the author(s) and should not be construed as an official Department of the Army position, policy, or decision, unless so designated by other documentation.

17.	COSATI CODES		18. SUBJECT TERMS (Continue on reverse if necessary and identify by block number)
FIELD	GROUP	SUB-GROUP	planar integrated circuits, microwave transmission

19. ABSTRACT (Continue on reverse if necessary and identify by block number)

The design and test of planar integrated circuits for the transmission and reception of microwave power are described. The circuits consist of MESFET transistor oscillators incorporating periodic microstrip antennas to form transmitters and transceivers. The nature of the periodic antennas allows their use as both resonant and radiating elements in the oscillator design, resulting in a simple and inexpensive circuit. The transmitter and transceiver circuits described here may be divided into two types; single device and dual device. The single device circuits use a single MESFET oscillating into a periodic microstrip patch antenna. The dual device circuits use two MESFETs which oscillate into a couple rampart line microstrip antenna. In the dual device circuit, the FETs may oscillate out of phase for power combining or in phase for frequency doubling. The transmitter circuits generate a beam of RF energy which radiates normal to the planar circuit surface. The transceiver circuits operate in a similar fashion, except that in this case, the antenna also acts to receive RF energy and direct it back to the oscillating MESFET. The MESFET then functions as a (cont'd)

20. DISTRIBUTION / AVAILABILITY OF ABSTRACT	21. ABSTRACT SECURITY CLASSIFICATION
☑ UNCLASSIFIED/UNLIMITED ☐ SAME AS RPT. ☐ DTIC USERS	Unclassified

22a. NAME OF RESPONSIBLE INDIVIDUAL	22b. TELEPHONE (Include Area Code)	22c. OFFICE SYMBOL
Tatsuo Itoh	(512) 471-1072	

(cont'd)

self-oscillating mixer for down-conversion of the received signal to the IF frequency. The low frequency IF is then extracted using a transformer.

Prototype circuits which operate a x-band are described and test results are given. The performance of the transmitters and transceivers is characterized using isotropic conversion gain, which accounts for the performance of the complete system, without breaking it into its sub-components. For the transmitter circuits, isotropic conversion gains from 5-9 dB are reported. For the transceiver circuits, the isotropic receiver gain is highly dependent on IF frequency and bias level, with a value above 5 dB reported. The use of the transceiver circuits for Doppler motion detection modules is also reported, and qualitative results are given.

Abstract

The design and test of planar integrated circuits for the transmission and reception of microwave power are described. The circuits consist of MESFET transistor oscillators incorporating periodic microstrip antennas to form transmitters and transceivers. The nature of the periodic antennas allows their use as both resonant and radiating elements in the oscillator design, resulting in a simple and inexpensive circuit. The transmitter and transceiver circuits described here may be divided into two types: single device and dual device. The single device circuits use a single MESFET oscillating into a periodic microstrip patch antenna. The dual device circuits use two MESFETs which oscillate into a coupled rampart line microstrip antenna. In the dual device circuit, the FETs may oscillate out of phase for power combining or in phase for frequency doubling. The transmitter circuits generate a beam of RF energy which radiates normal to the planar circuit surface. The transceiver circuits operate in a similar fashion, except that in this case, the antenna also acts to receive RF energy and direct it back to the oscillating MESFET. The MESFET then functions as a self-oscIlating mixer for down-conversion of the received signal to the IF frequency. The low frequency IF is then extracted using a transformer.

Prototype circuits which operate at x-band are described and test results are given. The performance of the transmitters and transceivers is characterized using isotropic conversion gain, which accounts for the performance of the complete system, without breaking it into its sub-components. For the transmitter circuits, isotropic conversion gains from 5 - 9 dB are reported. For the transceiver circuits, the isotropic

receiver gain is highly dependent on IF frequency and bias level, with a values above 5 dB reported. The use of the transceiver circuits for Doppler motion detection modules is also reported, and qualitative results are given.

TABLE OF CONTENTS

page

LIST OF FIGURES

x

LIST OF TABLES

CHAPTER 1: INTRODUCTION

In many microwave and millimeter-wave applications, it is advantageous to construct single components which perform several different functions, such as mixing, amplification, and signal detection. One example of this approach is the common CW Doppler radar module in which a single Gunn diode cavity oscillator serves to generate the transmitted signal and also to down convert the received Doppler-shifted signal [1]. Other examples of this approach are the so-called "quasi-optical" components, unique to millimeter wave work [2-5], which we will now describe.

At millimeter-wave frequencies, (which we can consider here to be frequencies in the range of 30 to 3000 GHz), the transmission of signals along conventional structures such as hollow waveguides or microstrip transmission lines may be impractical due to high loss. One way to solve this problem is by integrating antennas with each component in the millimeter-wave system, and therefore replacing the lossy transmission lines with free-space propagation, which is inherently a lower loss medium. These types of circuits are referred to as quasi-optical, since techniques similar to those used in optical systems are applicable, although circuit dimensions are of the order of only a few wavelengths. Many applications of this technique are reported in the literature, including quasi-optical mixers, transmitters, and frequency multiplying power combiners [6-10].

Complete systems using these techniques have also been reported [11].

In this work we describe the design and performance of MESFET based oscillator and transceiver circuits in which the resonant element in the oscillator performs a dual function as an antenna. In particular, the resonant element is a periodic

1

microstrip structure operated in the so-called "leaky-wave stop-band." In this configuration. the periodic structure will reflect a large portion of the input signal back towards the feed, while simultaneously radiating in the broadside direction. In this way, the oscillator and radiator functions are combined, and the resulting circuit may be termed a quasi-optical transmitter. This approach was inspired by the earlier work of Song and Itoh [12], in which the active device was a Gunn diode and the guiding structure was a periodically notched dielectric waveguide.

Three separate designs are reported here. In the first type, the periodic structure consists of a microstrip patch linear array, which is excited by a single FET. In the remaining two designs, the periodic structure consists of two coupled rampart line arrays, which are excited by two FETs. In this configuration, the performance of the circuit is determined by the phase of the oscillation of the two FETs. If the FETs oscillate in the odd mode, power is extracted at the fundamental frequency. If the FETs oscillate in the even mode. the power is extracted at the second harmonic frequency.

The transceiver circuits described here are very similar to the oscillators. and operate in the following way: When a received signal is injected into the oscillating FET, the FET behaves as a self-oscillating mixer, generating mixing products. Under the right conditions, the dominant mixing product will occur with a frequency equal to the difference of the received signal frequency and the oscillation frequency of the FET. In particular, if the received signal is a Doppler shifted version of the transmitted signal. then the mixing product will be at the Doppler frequency, and the circuit may be used as a type of radar.

In the second chapter we will describe the leaky-wave antennas using an idealized model, that of infinitesimal perturbations on a slow wave structure. This

analysis, although approximate, can give insight into the operation of these types of antennas.

In the third chapter, we describe the approximate small-signal oscillator design procedure used throughout this dissertation. We also give a very simple model of the MESFET which is used to show the origin of the negative resistance of the device. In addition, we derive an approximate formula for the optimum load impedance in terms of the small signal MESFET S-parameters.

In the fourth chapter, we describe in detail the operation of the single device oscillator circuit using the periodic patch antenna. We give the design process used and report on the oscillator performance for three separate oscillator circuits. In this chapter we introduce the concept of isotropic transmit gain and illustrate its use in comparing the performance of this type of oscillator circuit.

The fifth chapter focuses on the design and performance of the dual device modules. The principle of operation of the coupled microstrip rampart line antenna is given, and a procedure for its analysis is outlined. The application of this antenna to the push-push and push-pull oscillator circuits is detailed. Results for both types of circuits are given.

In the sixth chapter we describe the transceiver modules. The transceivers are of both single device and push-pull type. The single device transceiver uses the same antenna for both transmit and receive, with the received signal injected back into the drain of the FET. The dual device transceiver uses a separate receive antenna for injection of the received signal into the gate of the FETs. The low frequency IF signal is extracted using an IF transformer. The isotropic transmit and receive gains are

measured at an IF frequency of 5 - 15 GHz. The transceivers are then tested qualitatively for their application to Doppler motion detection purposes.

Conclusions are given in the seventh chapter, and applications for these circuits are given.

CHAPTER 2: PERIODIC STRUCTURES AND FLOQUET'S THEOREM

Each of the circuits described in this paper contain "almost periodic" structures as the resonant and radiating elements. The term "almost periodic" in this dissertation is taken to mean that the parameter of interest, the impedance, for each of the structures varies with a given period, but that the variation from period to period is not a constant. For example, in the case of the periodic microstrip patch array, the patch elements are each one half wavelength long (at the desired operating frequency), and the intervening sections are each one half wavelength long, but the impedance of the individual patch elements is not equal.

Although these structures are not strictly periodic, we main obtain insight into their operation by considering the propagation of waves along periodic guiding structures. An excellent description of this phenomenon is given in [13]; the remainder of this chapter follows this reference closely.

The description of guided waves travelling along an axially periodic structure is based on Floquet's theorem [13]. With the direction of propagation given as z, Floquet's theorem as it applies to our problem may be stated as follows: A time-harmonic electromagnetic field $\psi(x,y,z)$ of a normal mode guided along a structure which is periodic in the z-direction posses the property:

$$\psi(x,y,z+d) = e^{jk_{z0}d}\psi(x,y,z) \qquad (2.1)$$

Note that the electromagnetic field itself is not periodic. However, if we define the vector periodic function $P(x,y,z)$ in the following way:

5

$$P(x,y,z+d) = P(x,y,z),$$

we may express the electromagnetic field as

$$\psi(x,y,z) = e^{jk_{z0}z}P(x,y,z) \tag{2.2}$$

Equations (2.1) and (2.2) state that the complex field distribution of a periodic structure remains unchanged with translation of a distance d along the z direction, but that the amplitude is multiplied by a factor of $e^{jk_{z0}d}$. The periodic function $P(x,y,z)$ describes the local field structure within each period.

Since $P(x,y,z)$ is periodic with period d, we may expand it in a Fourier series as

$$P(x,y,z) = \sum_{n=-\infty}^{n=\infty} a_n(x,y)e^{j(2n\pi/d)z}$$

when this expression is substituted into (2.2) we get

$$\psi(x,y,z) = \sum_{n=-\infty}^{n=\infty} a_n(x,y)e^{jk_{zn}z} \tag{2.3}$$

where

$$k_{zn} = k_{z0} + 2n\pi/d \qquad n = \pm 1, \pm 2\ldots$$

The expression in (2.3) is known as the spatial harmonic expansion, and the individual terms $a_n(x,y)e^{jk_{zn}z}$ are referred to as the spatial harmonics. Each of the spatial harmonics represents a travelling wave with a propagation constant of k_{zn}, and an amplitude given by $a_n(x,y)$.

Although equation (2.3) appears similar to a conventional modal expansion for a waveguide, the two are quite different. In contrast with higher-order waveguide modes, the spatial harmonics do not individually satisfy the boundary conditions on the guide. Also, in a waveguide, the higher order modes are evanescent, while all of the spatial harmonics in (2.3) are unattenuated if k_{z0} is real.

The spatial harmonic representation lends itself to interpretation using the k_0d-βd diagram. This type of diagram is a graphical display of the dispersion relation of the guide. In Figure 2.1 we display the k_0d-βd diagram for the case of the periodically loaded, basically slow TEM structure in the limit of infinitesimal perturbation. Since the perturbation is infinitesimal, the individual dispersion curves are altered infinitesimally from the unperturbed case. Each of the lines in Figure 2.1 correspond to a spatial harmonic; the lines with positive slope indicate a forward traveling spatial harmonic, and negative slope indicates propagation in the backward direction.

The k_0d-βd plane is divided into two regions along the dashed lines at $k_0d = \pm \beta d$. The region above these lines is referred to as the fast wave region, since in this region $k_0 > \beta$. Below these lines, $k_0 < \beta$, and the spatial harmonics in this area represent bound waves. This is referred to as the slow wave region.

Let us examine a dispersion curve in Figure 2.1 for a particular spatial harmonic, say that for the backward wave with $n = -1$. For low frequencies, the curve lies in the slow wave region of the k_0d-βd diagram, and the spatial harmonic is bound.
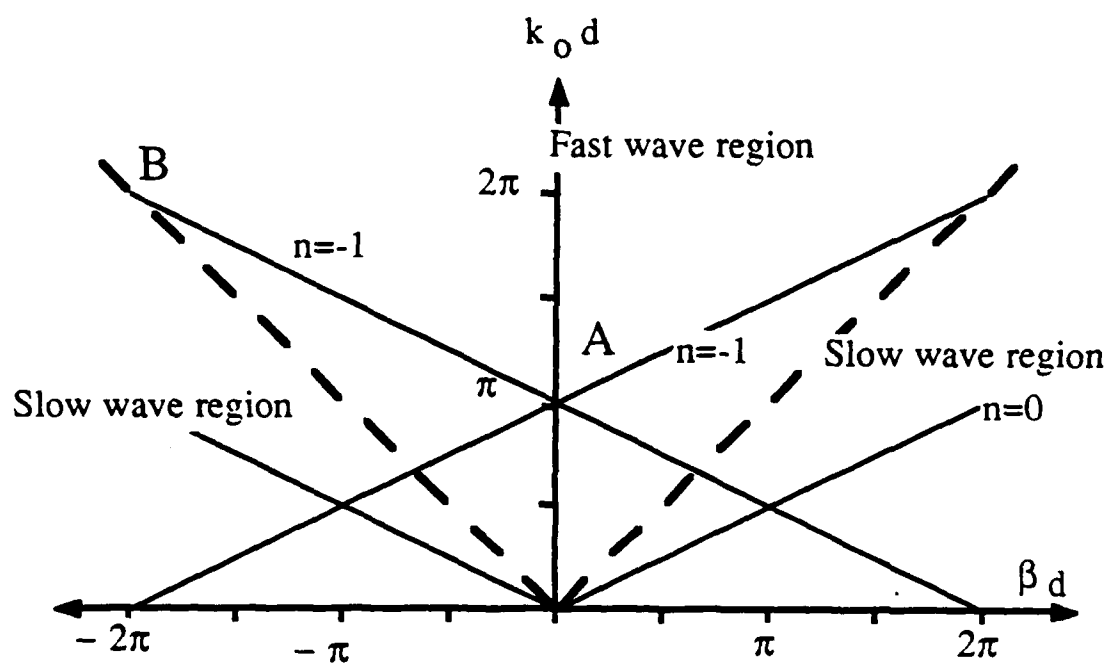
Figure 2.1   The $k_0 d$- βd diagram for the case of infinitesimal perturbations on a basically slow, TEM guiding structure.

As the frequency increases from zero, we approach the boundary of the fast wave region. When the line $k=\beta$ is reached, radiation from the open structure appears in the end-fire direction. As the frequency is increased further, the radiation sweeps around from end-fire towards broadside, with the radiation perpendicular to the axis of the guide when the point labeled A is reached. as the frequency is increased further, the radiation passes into the end-fire region, and finally reaches backfire at the point B.

Another feature which is apparent from Figure 2.1 is the degeneracy of the solutions. For this reason, the fundamental wave number may only be specified to within an integer multiple of $2\pi/d$.

The form of the dispersion curves for the same structure in the case of increased perturbation may be determined by applying the "mode coupling principle"[13]. Figure 2.2 shows one-half of the $k_0 d$-βd diagram for the same structure, except that the loading has now been increased and mode coupling has occurred at the points where the curves in Figure 2.1 have overlapped. In these regions, coupling between the forward and backward traveling spatial harmonics creates stop-bands, such as the two indicated by the points A and B.

As we increase the frequency from zero, the first stop-band encountered is that at A, due to the interaction of the $n = -1$ and $n = 0$ terms. In this case, all of the spatial harmonics exist in the slow wave region; therefore this stop-band is known as the surface wave stop-band.

As the frequency continues to increase, the next stop-band to be encountered is that at the point B, at approximately twice the frequency as the surface wave stop-band. This stop-band is due to the interaction of the $n=0$ and $n=-2$ spatial harmonics. Although this interaction occurs in the slow wave region of the diagram, at the same

Figure 2.2   The $k_0 d$-βd diagram for a basically slow, TEM guiding structure showing coupling between spatial harmonics.

time the n=1 and n=-1 spatial harmonics have entered the fast wave region of the diagram, and radiate in the broadside direction. This is the leaky-wave stop-band, and it is in this region that we are interested in operating.

The above description of periodic structures strictly applies only to TEM waves on infinite periodic basically slow structures. No account was taken of higher order modes, for example. Additionally, as is shown below, in the presence of certain symmetries, some of the stop-bands will not be present; more information on this phenomenon is given in [14].

One of the cases where the symmetry of the structure eliminates certain stop-bands is examined here. Consider the periodic transmission line shown in Figure 2.3, which consists of alternating sections of ideal lossless TEM transmission line. The transmission line sections alternate in lengths between l_A and l_B so that the length of one period is $l = l_A + l_B$. The impedance of the sections of length l_A is denoted Z_A and that of sections of length l_B denoted Z_B. In addition, we require that the electrical lengths of the sections are equal, that is $\beta_A l_A = \beta_B l_B$. Here we disregard any parasitic reactances due to possible discontinuities at the junctures of the lines. Although this example is somewhat artificial, it explains an effect seen later with the periodic patch array.

By Floquet's theorem (2.1) we may write for the voltage and current on the line

$$V(x+l) = e^{-j\gamma l}V(x)$$

$$I(x+l) = e^{-j\gamma l}I(x)$$
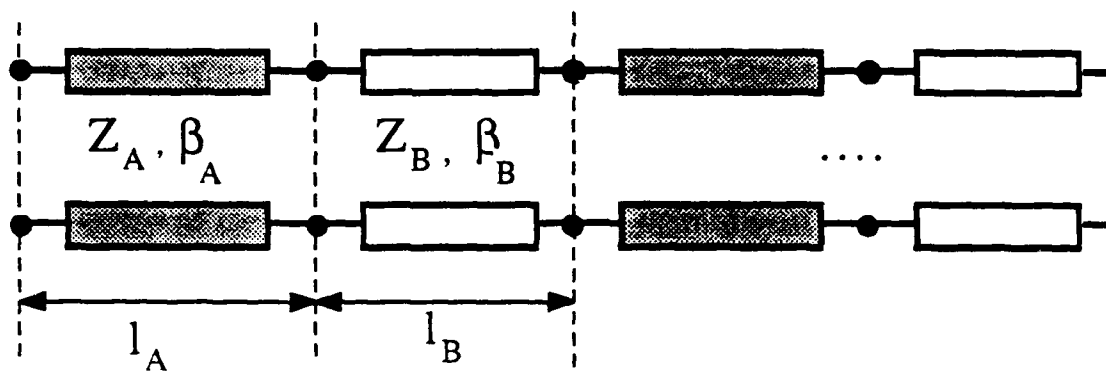
Figure 2.3   A periodic TEM transmission line with alternate sections
of equal electrical length.

where γ represents the unknown phase constant of the periodic structure and the negative sign in the exponential indicates a positive traveling wave. These relations may be expressed using the ABCD matrix for the unit cell as

$$\begin{bmatrix} V_n \\ I_n \end{bmatrix} = \begin{bmatrix} A_u & B_u \\ C_u & D_u \end{bmatrix} \begin{bmatrix} V_{n+1} \\ I_{n+1} \end{bmatrix} = e^{\gamma(l_A + l_B)} \begin{bmatrix} V_{n+1} \\ I_{n+1} \end{bmatrix} \tag{2.4}$$

where the subscript u indicates the unit cell.

The ABCD matrix for the unit cell which consists of the two lengths of line may be written as the product of the ABCD matrices for each individual length of line:

$$\begin{bmatrix} A_u & B_u \\ C_u & D_u \end{bmatrix} = \begin{bmatrix} A_A & B_A \\ C_A & D_A \end{bmatrix} \begin{bmatrix} A_B & B_B \\ C_B & D_B \end{bmatrix} = \begin{bmatrix} \cos\beta_A l_A & jZ_A \sin\beta_A l_A \\ \dfrac{j}{Z_A}\sin\beta_A l_A & \cos\beta_A l_A \end{bmatrix} \begin{bmatrix} \cos\beta_B l_B & jZ_B \sin\beta_B l_B \\ \dfrac{j}{Z_B}\sin\beta_B l_B & \cos\beta_B l_B \end{bmatrix}$$

$$= \begin{bmatrix} \cos\beta_A l_A \cos\beta_B l_B - \dfrac{Z_A}{Z_B}\sin\beta_A l_A \sin\beta_B l_B & jZ_A \sin\beta_A l_A \cos\beta_B l_B + jZ_B \cos\beta_A l_A \sin\beta_B l_B \\ \dfrac{j}{Z_A}\sin\beta_A l_A \cos\beta_B l_B + \dfrac{j}{Z_B}\cos\beta_A l_A \sin\beta_B l_B & \cos\beta_A l_A \cos\beta_B l_B - \dfrac{Z_B}{Z_A}\sin\beta_A l_A \sin\beta_B l_B \end{bmatrix}$$

Substituting this into Equation (2.4) gives an eigenvalue equation for the propagation constant γ:

$$\left(\begin{bmatrix} A_A & B_A \\ C_A & D_A \end{bmatrix} - \begin{bmatrix} e^{\gamma(l_A + l_B)} & 0 \\ 0 & e^{\gamma(l_A + l_B)} \end{bmatrix} \right) \begin{bmatrix} V_{n+1} \\ I_{n+1} \end{bmatrix} = 0$$

A unique solution exists when the determinant of the matrix in parentheses is zero:

$$\left| \begin{bmatrix} A_A B_A \\ C_A D_A \end{bmatrix} - \begin{bmatrix} e^{\gamma(l_A+l_B)} & 0 \\ 0 & e^{\gamma(l_A+l_B)} \end{bmatrix} \right| = A_u D_u - B_u C_u + e^{2\gamma(l_A+l_B)} - e^{\gamma(l_A+l_B)}(A_u + D_u) = 0$$

For a reciprocal network, AD-BC = 1, which gives:

$$\cosh\gamma l = \frac{A_u + D_u}{2} = \cos\beta_A l_A \cos\beta_B l_B - \frac{1}{2}\left(\frac{Z_A}{Z_B} + \frac{Z_B}{Z_A}\right)\sin\beta_A l_A \sin\beta_B l_B \qquad (2.5)$$

This is the dispersion relation for the periodic structure. When the expression on the right hand side is less than one, γ is imaginary, indicating a pass-band. Stop-bands occur when the expression on the right is greater than one. If we substitute $\beta_A l_A = \beta_B l_B$, we get:

$$\cosh\gamma l = \cos^2\beta_A l_A - \frac{1}{2}\left(\frac{Z_A}{Z_B} + \frac{Z_B}{Z_A}\right)\sin^2\beta_A l_A \qquad (2.6)$$

This term multiplying $\sin^2\beta_A l_A$ is always greater than one if $Z_A \neq Z_B$. Therefore, at the points where $\beta_A l_A = (2n-1)\pi/2$ we will have stop-bands. However, at $\beta_A l_A = n\pi$, in this case, we will not observe stop-bands. Therefore we will not see the leaky-wave stop-band described above, since this occurs where $\beta_A l_A = \pi$. However, this analysis does no take into account any discontinuity effects. We will consider this further when we discuss the microstrip periodic patch array.

Next, we examine the case shown in Figure 2.4 where the period is the same, but now one of the transmission line sections is three times longer than the other. An analysis similar to that given above shows that in this case, every fourth stop-band will be absent. Therefore, in this instance, the leaky-wave stop-band will be present.

In this chapter we have attempted to provide insight into the operation of the periodic antenna. We have described the radiation properties and demonstrated the existence of the stop-bands. However, as mentioned above, the structures used in our circuits are not strictly periodic. Therefore, although the above discussion can provide insight into the operation of the antennas, we will be required to use other approaches in the actual antenna design to determine the input reflection coefficient and the detailed radiation pattern. We will return to the analysis of the actual radiating structures later.
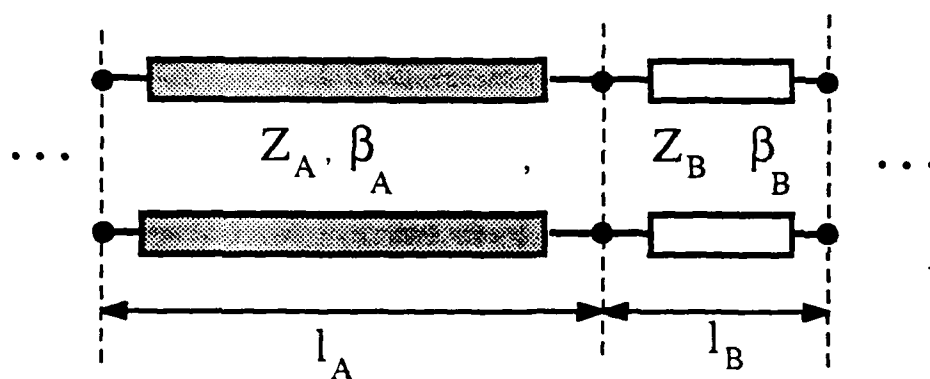
Figure 2.4   A periodic TEM transmisson line with alternating sections
              where $\beta_A l_A = 3\beta_B l_B$.

CHAPTER 3: OSCILLATOR DESIGN

The analysis and design of oscillator circuits may be undertaken using either of the following equivalent models shown in Figure 3.1: the loop feedback approach, or the negative resistance approach. The latter approach is most often used in the design of microwave oscillators.

The fundamental concepts in the design of microwave negative resistance oscillators have been described by Kurokawa [15,16]. In his approach, it is assumed that the impedance around the loop in the oscillator circuit may be divided into two parts: that which is a function only of the amplitude of the oscillation, $\overline{Z}(A)$, and that portion which is dependent only on the frequency of oscillation, $Z(\omega)$. The amplitude dependent portion has a negative real part, which accounts for the power generation. The locus of points of $\overline{Z}(A)$ when plotted on the complex impedance plane is referred to as the device line, and the locus of $Z(\omega)$ is referred to as the impedance line. The point of intersection of the two lines determines the amplitude and frequency of oscillation. At this point the oscillation condition is described by:

$$\overline{Z}(A_0) + Z(\omega_0) = 0$$

(3.1)

where

$$\overline{Z}(A) = \overline{R}(A) + j\overline{X}(A) \qquad \overline{R}(A) < 0$$

and $\qquad Z(\omega) = R(\omega) + jX(\omega)$

17
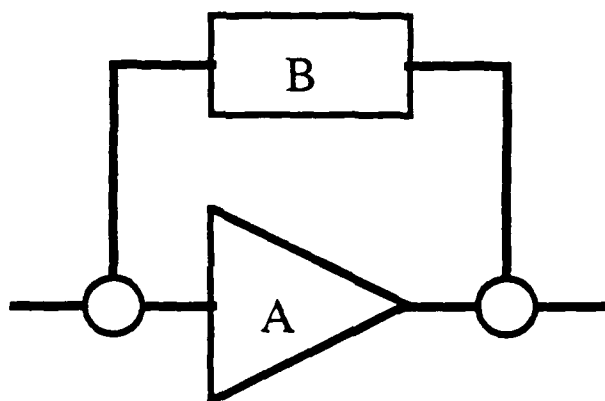
a)   AB = -1
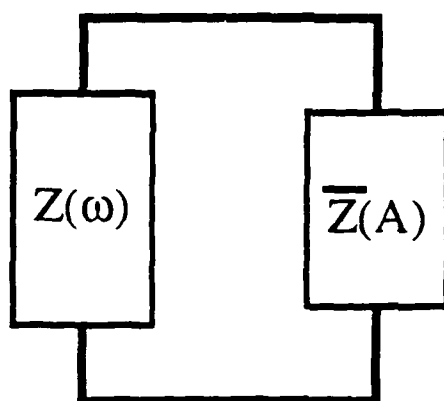
b) $Z(\omega) = -\overline{Z}(A)$

Figure 3.1   Two approaches to the oscillator problem: a) feedback approach; b) negative resistance approach.

and the subscript 0 indicates that the oscillation condition is satisfied. This indicates that in the steady-state, the real part of the device impedance is exactly balanced by that of the resonator, and similarly for the imaginary part. While this condition obtains at steady-state, it does not indicate what conditions on the device and the resonant structure provide stable operation at the point at which maximum power is extracted from the device. Determination of these properties requires detailed knowledge of the non-linear parameters of the device [17,18]; we will return to this shortly.

In order to facilitate the design procedure, it is convenient to express the oscillation condition given in (3.1) in a different form. We may express the reflection coefficients of the active device and the load as

$$\overline{\Gamma} = \frac{\overline{R} + j\overline{X} - Z_0}{\overline{R} + j\overline{X} + Z_0}$$

and

$$\Gamma = \frac{R + jX - Z_0}{R + jX + Z_0},$$

where Z_0 is the characteristic impedance of the system. Taking the product of $\overline{\Gamma}$ and Γ gives:

$$\overline{\Gamma}\Gamma = \frac{\overline{R} + j\overline{X} - Z_0}{\overline{R} + j\overline{X} + Z_0} \times \frac{R + jX - Z_0}{R + jX + Z_0}$$

If we substitute the condition for oscillation of equation (3.1),

$$\overline{R}(A_0) = -R(\omega_0) \qquad \text{and} \qquad \overline{X}(A_0) = -X(\omega_0)$$

we get

$$\overline{\Gamma\Gamma} = \frac{- R(\omega_0) - jX(\omega_0) - Z_0}{- R(\omega_0) - jX(\omega_0) + Z_0} \times \frac{R(\omega_0) + jX(\omega_0) - Z_0}{R(\omega_0) + jX(\omega_0) + Z_0}$$

The numerator of the second term is equal to -1 times the denominator of the first term, and vice-versa. Thus an expression equivalent to (3.1) which indicates the oscillation condition is given by:

$$\overline{\Gamma\Gamma} = 1 \qquad\qquad (3.2)$$

Note that $\overline{\Gamma}$ and Γ are complex quantities; (3.2) specifies the magnitude and phase of their product.

It is appropriate at this point to illustrate that the MESFET, when properly configured, may be considered as a one-port negative resistance element. To this end we consider Figure 3.2. This is a simple small signal equivalent circuit for a typical MESFET [17], which we may use to show the possibility of negative resistance behavior. By terminating the gate port in a reactance B_g and connecting the source to ground, we obtain the equivalent circuit shown in Figure 3.3. We may determine the admittance seen "looking into" the drain by calculating the gate voltage, V_g, in terms of the drain voltage, V_d,

$$V_g = \frac{\omega C_{dg}}{B_g + \omega C_{gs} + \omega C_{dg}} V_d$$
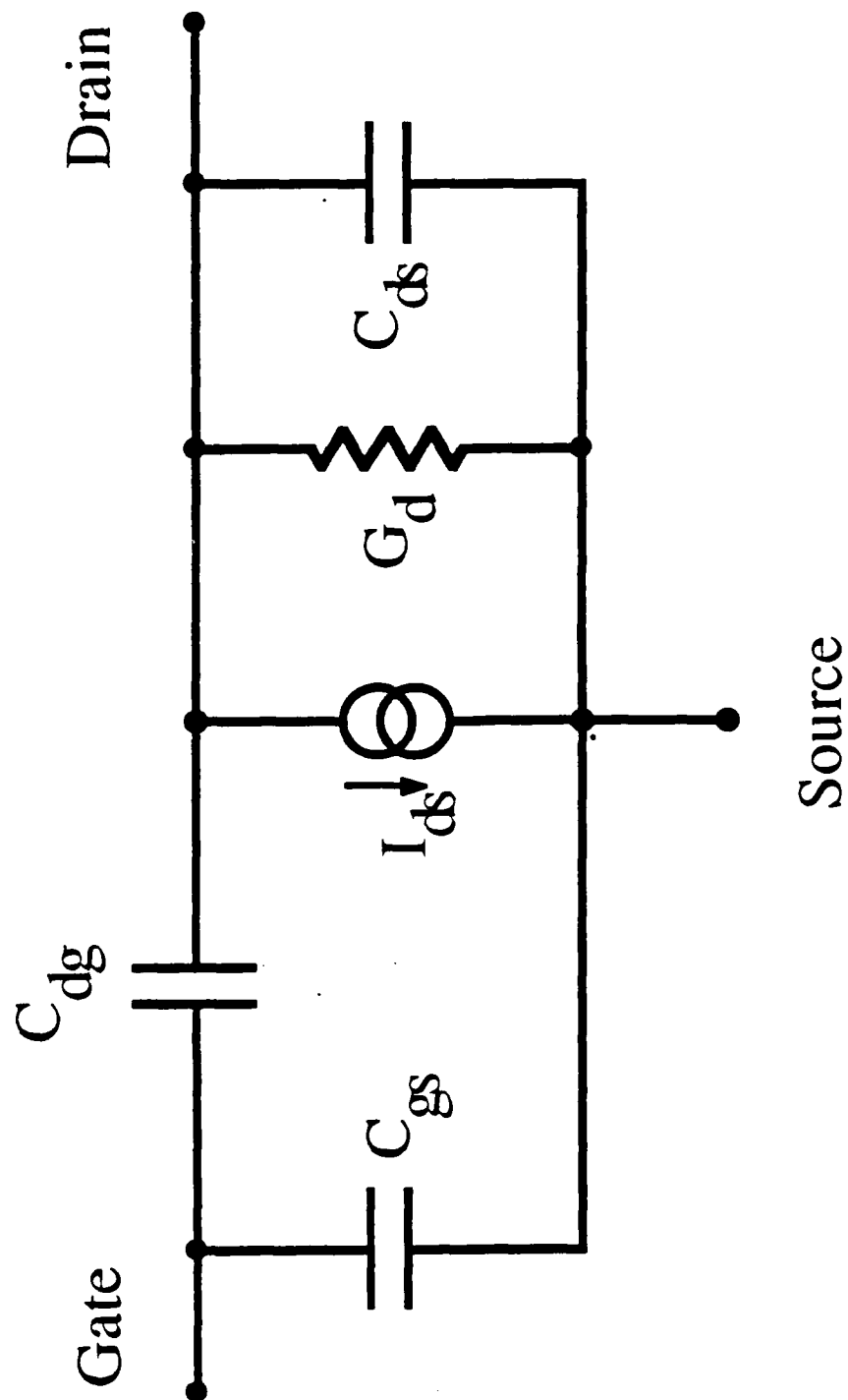
Figure 3.2 A small signal equivalent circuit for the MESFET.
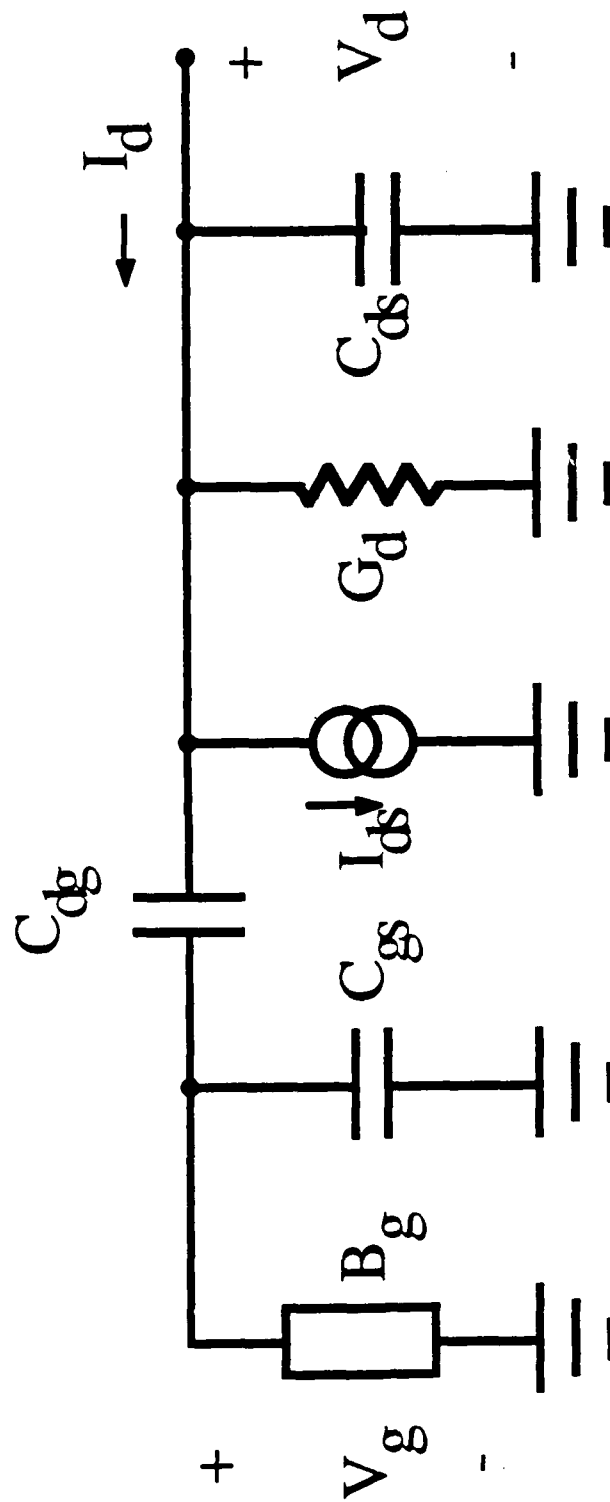
Figure 3.3   The circuit formed from the small signal MESFET circuit with the source grounded and a susceptance attached to the gate.

Noting that

$$I_{ds} = g_m V_g$$

and substituting into the current equation at the drain node, we get:

$$Y_d = \frac{I_d}{V_d} = \frac{\omega g_m C_{dg}}{B_g + \omega C_{gs} + \omega C_{dg}} + G_d + j\omega \left[C_{dg}\left(\frac{B_g + \omega C_{gs}}{B_g + \omega C_{gs} + \omega C_{dg}} \right) + C_{ds} \right] \quad (3.3)$$

This shows that, depending on the value of B_g, the admittance at the drain port can have a negative real part. In addition, since the MESFET has a Schottky Barrier type gate terminal, C_{gs} may be varied by adjusting the gate dc bias voltage. This in turn will affect both the magnitude and phase of Y_d, and therefore alter both the operating frequency and output power of the oscillator. In practice, an additional feedback element may be added in series with the source of the MESFET to further enhance the negative resistance. Note that no nonlinear elements are used in this approximate analysis, so that it cannot be used to predict any steady-state behavior of the oscillator. Nevertheless, we expect the results to be valid for the small signal case.

The design of the oscillators described in this dissertation proceeds using small signal parameters and linear equivalent circuits with the Touchstone™ microwave CAD program available from EESof Corporation of Westlake Village, CA.

The design procedure follows, where we assume throughout that the parameters of the periodic antenna and hence the desired operating frequency have been determined in advance. The first step is the selection of the transistor. It is desirable to choose a

transistor with sufficient gain and output power at the intended frequency of operation. This is determined by examination of the manufacturer's data sheets. For the purpose of the demonstration of concept desired here, almost any small-signal commercially available X-band MESFET will suffice.

Secondly, the values of the gate and source terminations for the transistor which result in negative impedance at the drain port must be determined. Although the MESFET small signal equivalent circuit from the above derivation may be used for this purpose, it is more convenient to use the following approach based on the stability of two-port networks.

For the moment, let us consider the MESFET and its external source termination as a two-port network with the gate and drain being the ports, as shown in Figure 3.4. The problem now becomes, in S-parameter representation, the determination of values of reflection coefficient at the gate port, Γ_g, which will result in the magnitude of the reflection coefficient at the drain port, S_{22}' to be greater than unity. It may be shown that the locus of values of Γ_g that result in $S_{22}' = 1$, when plotted on the Smith chart, forms a circle centered at

$$C = \frac{(S_{22} - D(S_{11})^*)^*}{|S_{22}|^2 - |D|^2}$$

with radius

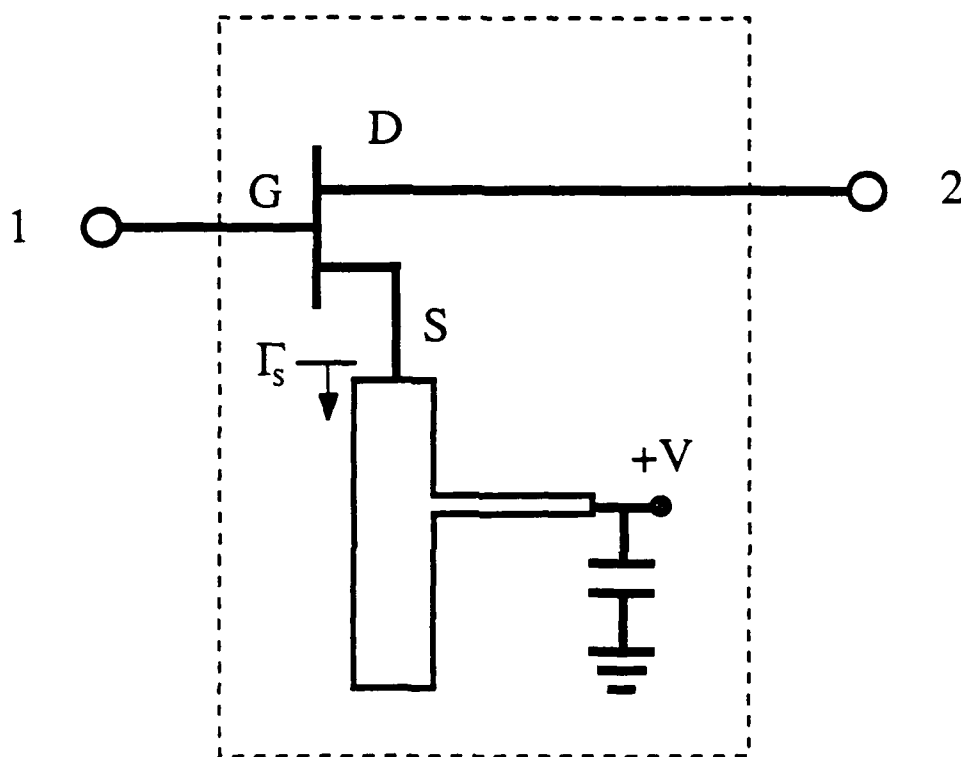$$r = \frac{|S_{12}S_{21}|}{\left||S_{22}|^2 - |D|^2\right|}$$

Figure 3.4   Equivalent two-port network for the determination of gate
and source terminating admittances.

where $D = S_{11}S_{22} - S_{12}S_{21}$, and the star indicates complex conjugate. This is known as the output stability circle of the two-port. If the magnitude of S_{22} of the original two-port is less than one, the interior of this circle represents an unstable operating point, which is desired for oscillation. An output stability circle for an NEC-71083 MESFET with the source grounded at 10 GHz appears in Figure 3.5. This plot was generated using Touchstone™.

Now we may proceed with the design. Having selected the MESFET, we use the S-parameters provided by the manufacturer in the remainder of the design steps. By attaching to the source terminal a simple circuit element, such as an open- or short-circuited microstrip line, we may construct the two-port circuit shown in Figure 3.4. We may plot the output stability circles of this two-port as a function of the parameters of the circuit attached to the source. We desire to cause the output stability circle to overlap the Smith chart as shown in Figure 3.6, where we have plotted the stability circle position as a function of source short circuit stub length for an NEC-71083 with a short circuit stub on the source.

Once the source circuit has been chosen so that the output stability circle overlaps some portion of the Smith chart, we choose the gate circuit so that its admittance falls inside the circle, insuring that the output admittance has a negative real part. In most cases, the circuit on the gate can be a simple microstrip element also. In some cases, however, the gate circuit needs to be more complicated. This is because of the nature of the MESFET and the periodic antenna. Since we wish to operate in the second stop-band of the antenna, we must avoid oscillation in the first stop-band. However, the gain of the MESFET increases as the frequency decreases, so that the device becomes less stable at lower frequencies. The result is in many cases, the device
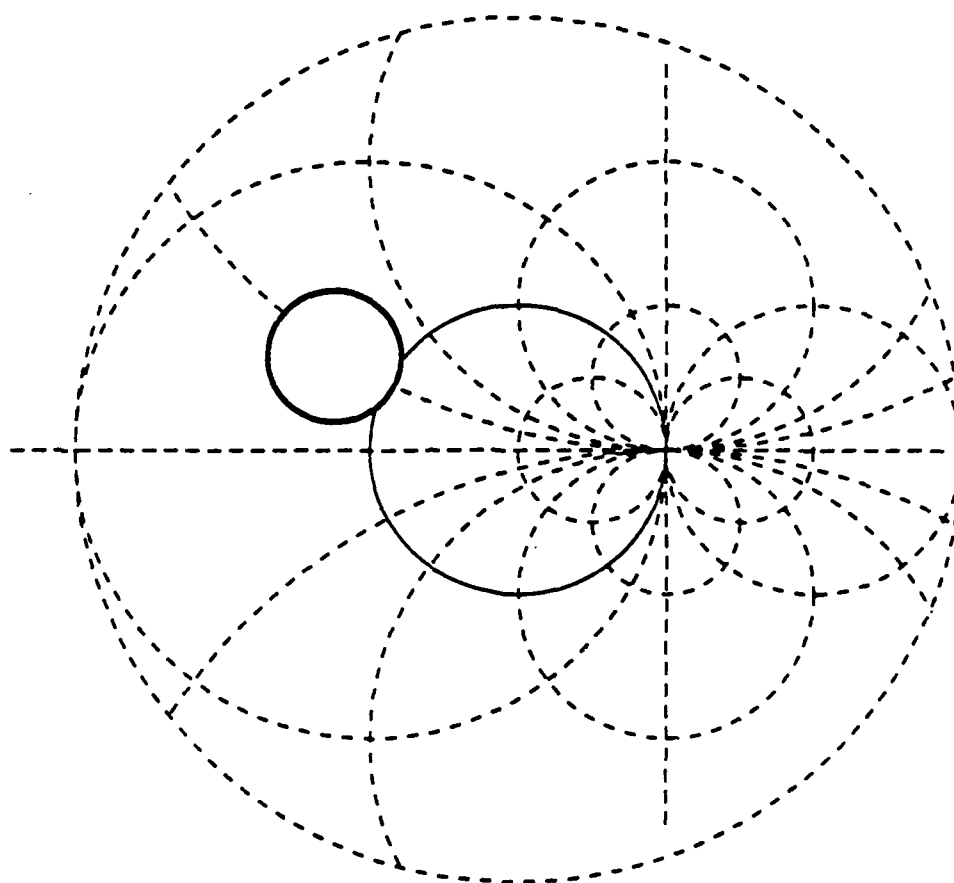
Figure 3.5 Output stability circle for NEC-71083 packaged MESFET
in the common-source configuration at 10 GHz.
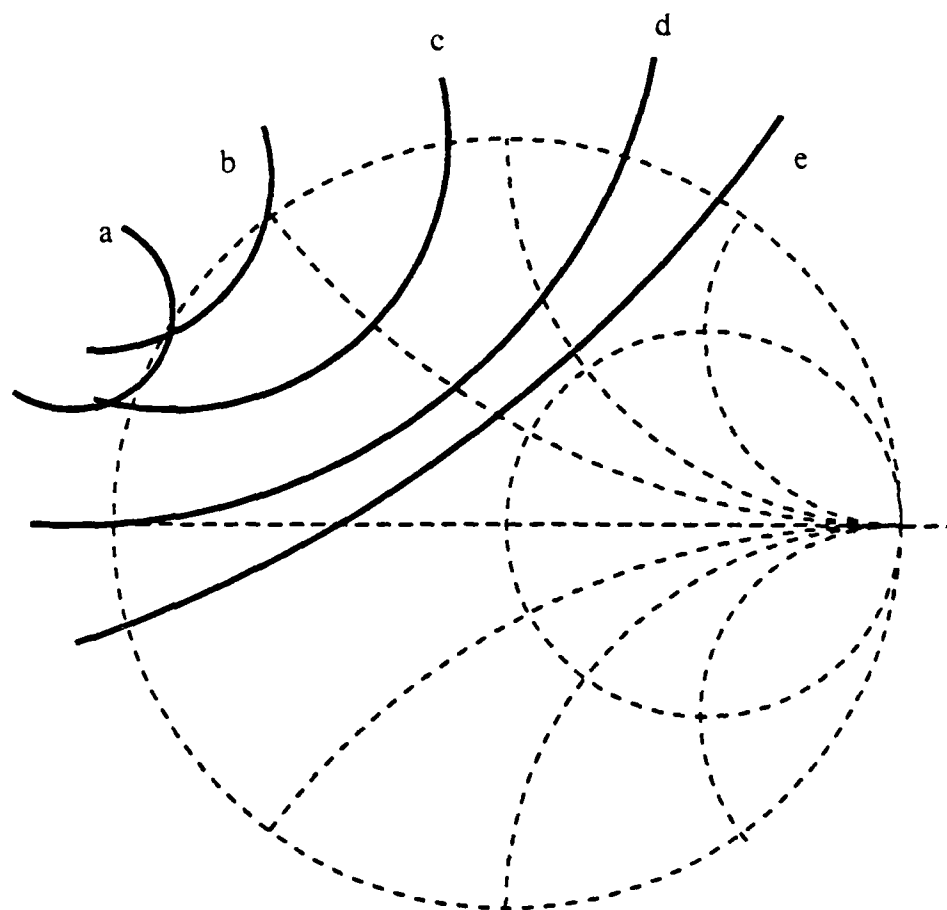
Figure 3.6   A family of output stability circles for the NEC-71083
              MESFET as a function of source termination.

a) $\Gamma_s = -1.0$

b) $\Gamma_s = -.98 + j.22$

c) $\Gamma_s = -.90 + j.43$

d) $\Gamma_s = -.79 + j.61$

e) $\Gamma_s = -.65 + j.76$

will tend towards oscillation at the lowest possible frequency. In order to control this problem, a low pass filter may be placed on the gate of the device. The low pass filter must be designed so that the desired oscillation frequency is in its stop-band region. The phase of the reflection coefficient at this frequency may be adjusted using an intervening section of microstrip line so that it falls within the unstable operation region defined by the output stability circle. At the same time, it must appear as a nearly matched termination at frequencies within the surface wave stop-band of the periodic structure which will be attached at the drain port.

It is also very important in the design of the source and gate circuitry to take into account the eventual biasing of the transistor. However, since the bias scheme is different for each of the circuits considered in this dissertation, we will reserve discussion on this subject for later chapters.

Once the source and gate terminating networks have been chosen, the MESFET may now be considered to be a one-port negative resistance element, and the design techniques pertaining to negative resistance oscillators may be used. It was mentioned above that Equation (3.1) applies to steady-state operation only. The negative resistance calculated from (3.3) or the Touchstone™ model applies only to the very small oscillation amplitudes which are present at the beginning of the oscillation, and not to the value which is present once steady-state is reached. To accurately predict the value of the negative resistance in this case, precise large-signal models or measured data must be used.

By using an approximate analysis, we may get an idea of how to select the admittance of the load so that oscillation will commence and reach a steady-state value where the negative resistance element will deliver maximum power to the load. To

begin with, we assume that the non-linear negative resistance behavior of the MESFET

may be approximated by a cubic polynomial as shown in Figure 3.7. The dynamic

conductance is given by the derivative of the current with respect to the voltage.

Therefore, if the instantaneous value of the current is given by

$$I = -a_1V + a_3V^3$$

then the dynamic conductance is

$$G = -a_1 + 3a_3V^2$$

For the single frequency case we may calculate the generated power by assuming that

the only voltage present across the negative resistance element is given by

$$V = \sqrt{2}V_0\cos\omega t$$

and calculate the power using

$$P = \frac{1}{T} \int_0^T I*V \, dt$$

which gives

$$P = -a_1V_0^2\left(1 - \frac{3}{2}\frac{a_3}{a_1}V_0^2\right),$$

where the negative sign indicates that power is being generated.

We may use this expression to define the effective negative conductance as
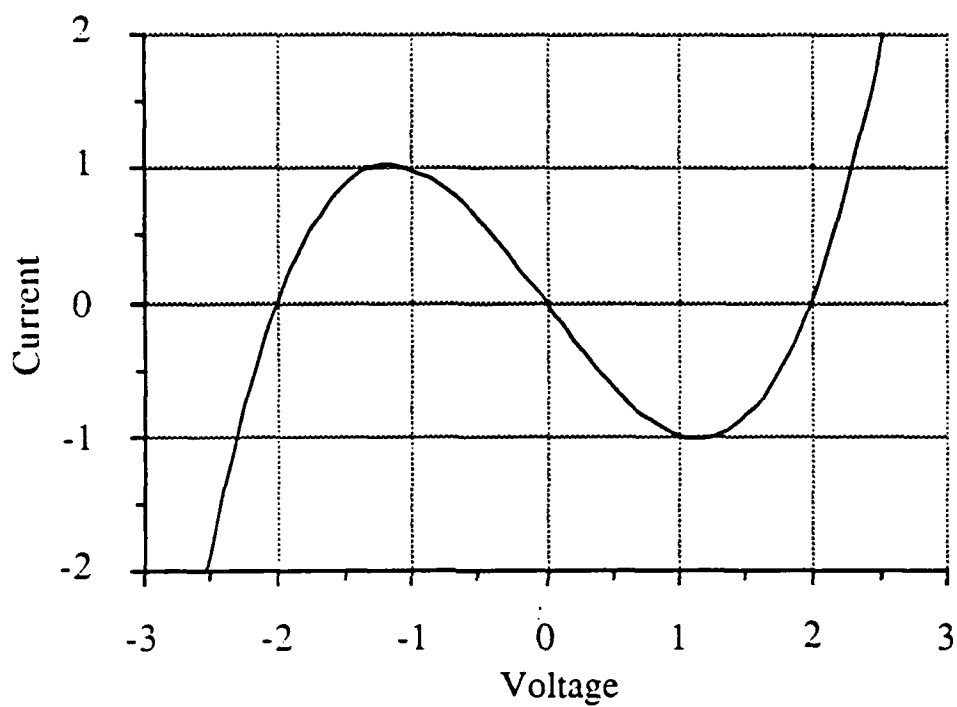
Figure 3.7   Cubic approximation of output current as a function
of applied voltage for a negative resistance device.

$$G_{eff} = - a_1 \left(1 - \frac{3}{2} \frac{a_3}{a_1} V_0^2 \right)$$

This value is the average conductance that appears in response to an applied voltage of V_0 (rms). If we call the small signal value of the negative conductance G_0, we eliminate one of the unknowns to get

$$G_{rms} = G_0 \left(1 - \alpha V_0^2 \right)$$

where $\alpha = (3/2)(a_3/a_1)$, and $G_0 < 0$.

In the steady-state we have, from (3.1)

$$G_0 \left(1 - \alpha V^2 \right) = - G_L \qquad (3.4)$$

where G_L is the conductance of the load. hence the power emanating from the negative resistance becomes

$$P = - G_L V^2 = G_0 \left(1 - \alpha V^2 \right) V^2 \qquad (3.5)$$

Taking the derivative of this expression with respect to V and setting the result equal to zero gives V_m. the value of V for which the output power is maximized:

$$V_m = \frac{1}{\sqrt{2\alpha}}$$

If we substitute this value into (3.4), we get

$$G_L = \frac{1}{2}|G_0|$$

(3.6)

Therefore, using this approximate method, we predict that the optimum power output is achieved when the output circuit conductance is set to one-half of the small-signal value of negative conductance of the active device. Furthermore, if we solve (3.4) for V^2 and substitute into (3.5) we get

$$P = -\frac{G_L}{\alpha}\left(1 + \frac{G_L}{G_0}\right)$$

This expression is quadratic in G_L, with the expected maximum at $G_L = |G_0/2|$, but most importantly the first derivative with respect to G_L is equal to zero at the maximum, which indicates that the value for G_L is not critical.

Based upon the above approximate analysis, it is determined that, at the design frequency, the small signal negative admittance of the MESFET circuit as predicted by Touchstone™ and the input admittance of the antenna should be in the relation given by (3.6). Using Touchstone™, we may adjust the length of the short circuit stub on the gate of the MESFET to cause this to take place.

At this point, then, we have determined the values for the gate and source terminations of the MESFET so that the admittance of the drain port obeys the following "start-up" conditions:

$$G_L = |G_0/2| \quad \text{and} \quad B_L = -B_0$$

The final step in the design of the oscillator circuit is ensuring that the oscillation condition is only satisfied at the design frequency. With Touchstone™, we may form the product of the S-parameters of two independent networks, as long as they have the same number of ports. Using this feature, we may compute the product given in equation (3.2) and plot the result as a function of frequency on the Smith chart. Wherever the locus encircles the point (1,0), corresponding to open circuit conditions, a possible oscillation is indicated. Using this method, the gate and source terminations may be adjusted so as to eliminate any possibility of the circuit oscillating at any point other than the desired one, paying special attention to the surface wave stop-band.

It is necessary to mention that the actual design flow is not as linear as may be imagined from the above description. In reality, it is often determined part way through the process that the particular topology being used is not adequate, for example, or that the given antenna is not adequate for the job. In these cases, the designer may make adjustments as the design dictates.

CHAPTER 4: THE SINGLE DEVICE OSCILLATOR

The single device oscillator is constructed using a periodic microstrip patch array as shown in Figure 4.1. This antenna consists of microstrip patches of varying width of length $\lambda_p/2$ separated by sections of 50 ohm line of length $\lambda_m/2$, where λ_p is the guide wavelength in the patch and λ_m is the guide wavelength in the 50 ohm microstrip line, at the desired operating frequency. The structure is terminated in a 50 ohm resistor.

The radiation from the individual patch elements may be explained using the cavity model developed by Lo, et. al. [20]. In this model, the rectangular microstrip patch is modeled as a thin cavity with perfectly conducting surfaces replacing the top metallization and ground plane, and a magnetic wall around the periphery. It is assumed that there is no field variation in the direction normal to the patch, $(d/dz = 0)$. This is justified by noting that, for thin substrates, the fields are largely confined to the region under the patch, and nearly zero elsewhere. In addition, the length and width of the patch may be replaced by the effective dimensions to take into account the presence of the fringing fields [21]. The fields in the cavity due to excitation from the microstrip feed may then be represented by an expansion in terms of the cavity modes, which may be seen to correspond to the TM modes for a rectangular waveguide. At the frequency where the length of the patch is near to $\lambda_p/2$, we expect that the amplitude of the TM_{10} mode to be dominant.

The radiation due to the fields under the patch is calculated by applying Huygens' principle to the outer surface of the cavity and neglecting the electric currents. The Huygens' sources on the magnetic wall are then given by
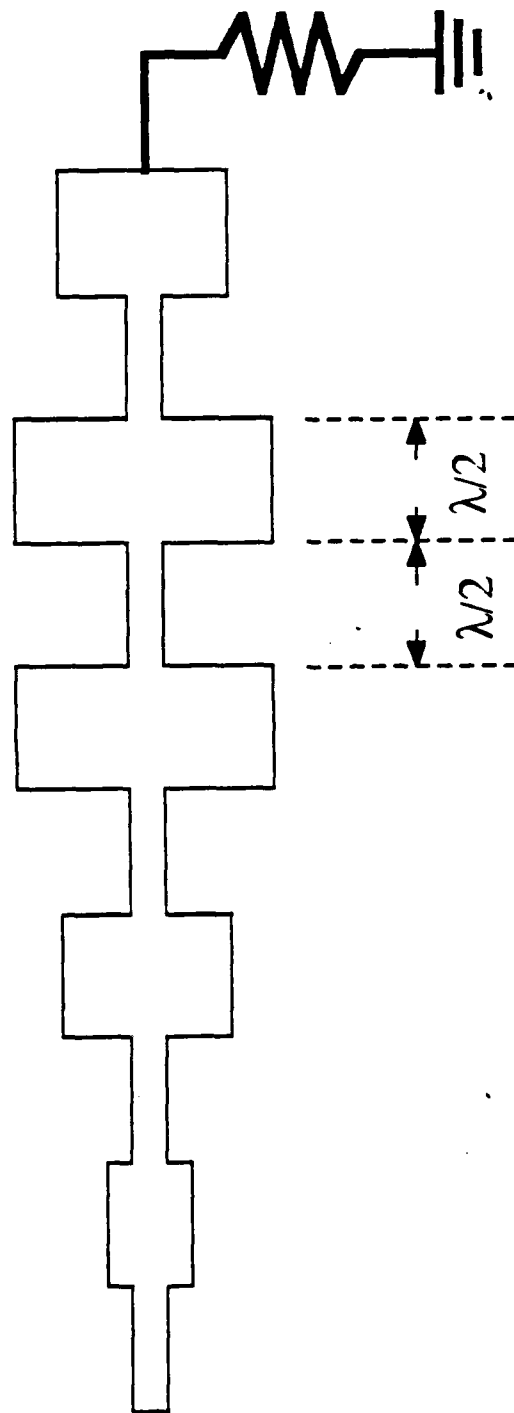
35

Figure 4.1 The microstrip patch linear array.

$$\vec{K} = 2\,\hat{n} \times \hat{z}\,E_Z$$

where $\vec{K}$ represents the magnetic current on the magnetic wall. $\hat{n}$ is the outward normal to the wall, and the factor of two accounts for the image in the ground plane. The radiated fields are then found by integrating over these magnetic currents in free space. For the TM_{10} case, the magnetic currents at the opposite ends of the patch are oriented in the same direction, while those along the sides of the patch will oppose each other. Thus, the E-plane is along the length of the patch. The antenna admittance is then found by summing the purely reactive admittance of the lossless cavity and the real radiation admittance which is determined by integration over the far field. Note that this approach does not take into account the generation of surface waves in the substrate. However, it has been determined that for substrate material with $\varepsilon_r \sim 10$, the surface wave excitation will become appreciable only when the dielectric thickness is greater than $0.03\lambda_0$ [22]. We will operate below this limit.

By concatenating several of these patches into an array with interconnects made by use of microstrip lines of length $\lambda_m/2$, we create an antenna which exhibits a maximum in the broadside direction. In addition, although it is a periodic structure, the arguments of Chapter Two would have us believe that there will not be any stop-band at this operating point, since the electrical length of each section is π. In fact, the stop-band does exist, and it is due to the discontinuities at the junctions between the patches and the feed lines. It is this stop-band that forms the basis for our oscillator circuit.

The discontinuities introduced at the junctions may be analyzed using the planar waveguide model [23,24], which does not take into account radiation. Sorrentino and

Pileri have demonstrated an alternative approach to account for the radiation loss [25]. For our purposes, one alternative is to proceed using a model which does not account for radiation to establish the voltage on the structure. Having determined the voltage at each step, we may then calculate the radiation using Huygens' principle as described above.

The model used in Touchstone™ for the microstrip step discontinuity is derived from the planar waveguide model, which results in the equivalent circuit shown in Figure 4.2. If the radiation loss were included, it would appear as the resistance R_{rad} shown in the dashed lines, however, this is not included in the Touchstone™ model. The voltage at each radiating step is found from the computer model by forming the equivalent circuit for the patch array, including discontinuities, and calculating the Thevenin equivalents at each step. The input return loss is simultaneously calculated.

Once the voltage at each step is known, the overall radiation pattern for the array may be calculated by multiplying this value by the radiation pattern for the two equivalent magnetic currents on either side of the feed, as shown in Figure 4.3.

To determine the validity of the above approach, we can include the resistor shown in Figure 4.2., by using the approximation for the radiation conductance of the open-end microstrip given in [26]:

$$G_r = \frac{w_e^2}{90 \, \lambda_0^2}$$

where w_e is the width of the microstrip patch and λ_0 is the free space wavelength. This expression does not take into account the radiation from the step discontinuity . It has
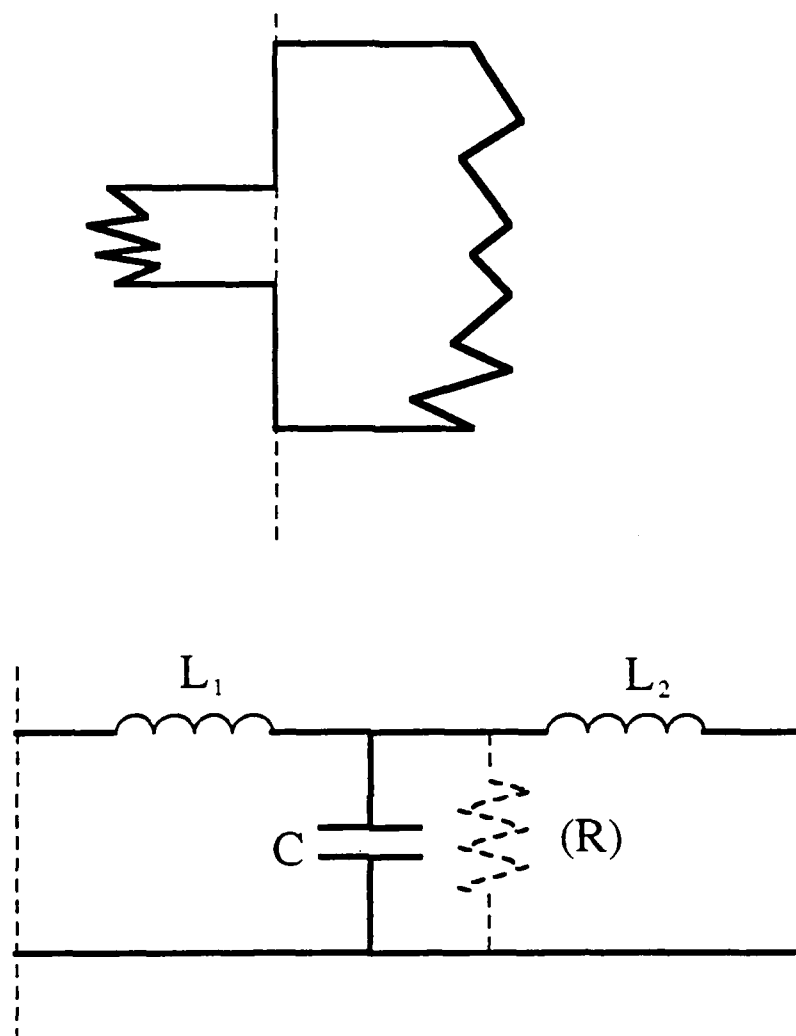
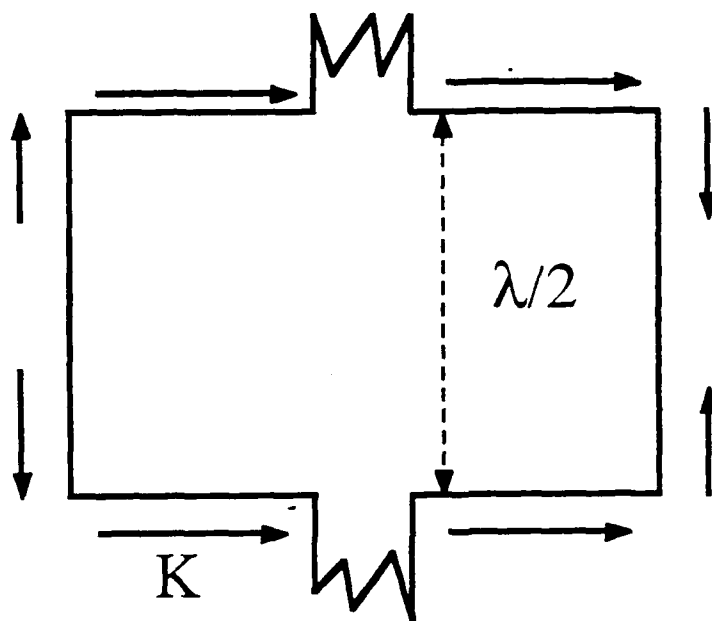Figure 4.2. The equivalent circuit for the microstrip step discontinuity.

Figure 4.3. The microstrip patch showing equivalent magnetic currents.

been estimated that the radiated power due to this discontinuity is about one third that of the patch itself [27]; this should not cause a problem considering the approximate nature of this analysis. At any rate, when the equivalent circuit for the antenna given by Touchstone™ is modified by adding the above radiation conductances at the step discontinuities, the effect on the standing wave amplitudes at the radiating discontinuities is very slight, approximately 2% in the worst case. This demonstrates that the voltage distribution along the antenna is primarily due to the reflections from the discontinuities and is only slightly affected by radiation.

From the above observations it was determined that the best approach for the design of the oscillator was to use Touchstone™ to model the antenna using the standard microstrip discontinuity models from [24], and not taking into account radiation loss. Once an antenna profile which appeared to be satisfactory from the point of view of a resonant structure was determined using this approach, the antenna performance could be modeled using the magnetic current approach as described above.

First we concentrate on the design of the patch array as a resonant structure. From equation (2.5) we see that the band-edges of the first stop-band of the antenna are determined from the points where

$$\cos^2\beta_A l_A + \frac{1}{2}\left(\frac{Z_A}{Z_B} + \frac{Z_B}{Z_A}\right)\sin^2\beta_A l_A = 1$$

for the lowest two values of $\beta_A \neq 0$. Since this occurs where $\beta_A l_A \sim \pi/2$, we have $\cos^2\beta_A l_A \sim 0$. Therefore, the surface-wave stop-band width is primarily determined by the ratio of Z_A to Z_B. For the patch array, this ratio will be around 4 or 5 for efficient radiators, with the impedance of the patches of the order of 10 ohms for a

substrate height of 0.635 mm and a relative dielectric constant of 10.2. Therefore, we expect a very broad surface-wave stop-band. This can be a problem, since it may cause the circuit to oscillate at these undesired frequencies.

Practical design rules for the individual patch elements may be taken from [21]. The first step is determination of the element width using the cavity model described above. If the patch is too narrow, the width of the radiating apertures is to small, and the radiated power drops. If the patch is too wide, undesired modes may be excited. A rule of thumb for the width is:

$$W = \frac{c}{2f_r} \left(\frac{\epsilon_r + 1}{2} \right)^{-\frac{1}{2}}$$

which is near to a half wavelength.
The length is then calculated from

$$L = \frac{c}{2 f_r \sqrt{\epsilon_{eff}}} - 2\Delta l$$

where ϵ_{eff} is the effective dielectric constant for the microstrip of width W, and Δl is the effective length extension for the patch due to fringing fields. Expressions for these quantities are taken from empirical relations [28]:

$$\epsilon_{eff} = \frac{\epsilon_r + 1}{2} + \frac{\epsilon_r - 1}{2} \left(1 + \frac{12h}{W} \right)^{-\frac{1}{2}}$$

$$\frac{\Delta l}{h} = 0.412 \frac{\left(\varepsilon_{eff} + 0.3\right)\left(\frac{W}{h} - 0.264\right)}{\left(\varepsilon_{eff} - 0.258\right)\left(\frac{W}{h} + 0.8\right)}$$

where h is the height of the dielectric. Note that this approach does not consider the effects of the step junction discontinuities on the performance of the patch radiators.

The above design rules were used to create microstrip arrays first using equal dimension patches along the length of the array. However, for this type of structure, it was found that the filter characteristics are quite poor, with very large ripple in the pass-bands, and a pass-band return loss of only about 3 dB. For the oscillator circuit, this means that it becomes quite difficult to control the frequency, since the oscillation condition may be satisfied at several different frequencies in this case. It was determined empirically that the best performance would be obtained by varying the width of the patch elements, starting with narrower patches at the ends of the array and gradually widening the patches toward the center of the array, where the middle patches would be of the size described above. In this case, pass-band response improves on either side of the stop-band, making the antenna more appropriate as a reflector. In Figures 4.4 and 4.5, the calculated and measured return loss for a 17 element patch array are plotted. Rogers Duroid 6010.2 with a relative dielectric constant of 10.2 and height of 0.635 mm was used. The three centermost patch elements measured 6.35 mm wide by 4.90 mm long. The widths of the remaining patches vary in steps of 0.762 mm from 1.27 mm for the end patches to 5.84 mm near the center.

The synthesis of this type of array structure is complicated. The width of the patch elements determines not only the voltage pattern along the array, but also the radiation from each element. This is not the case in the coupled meander line array
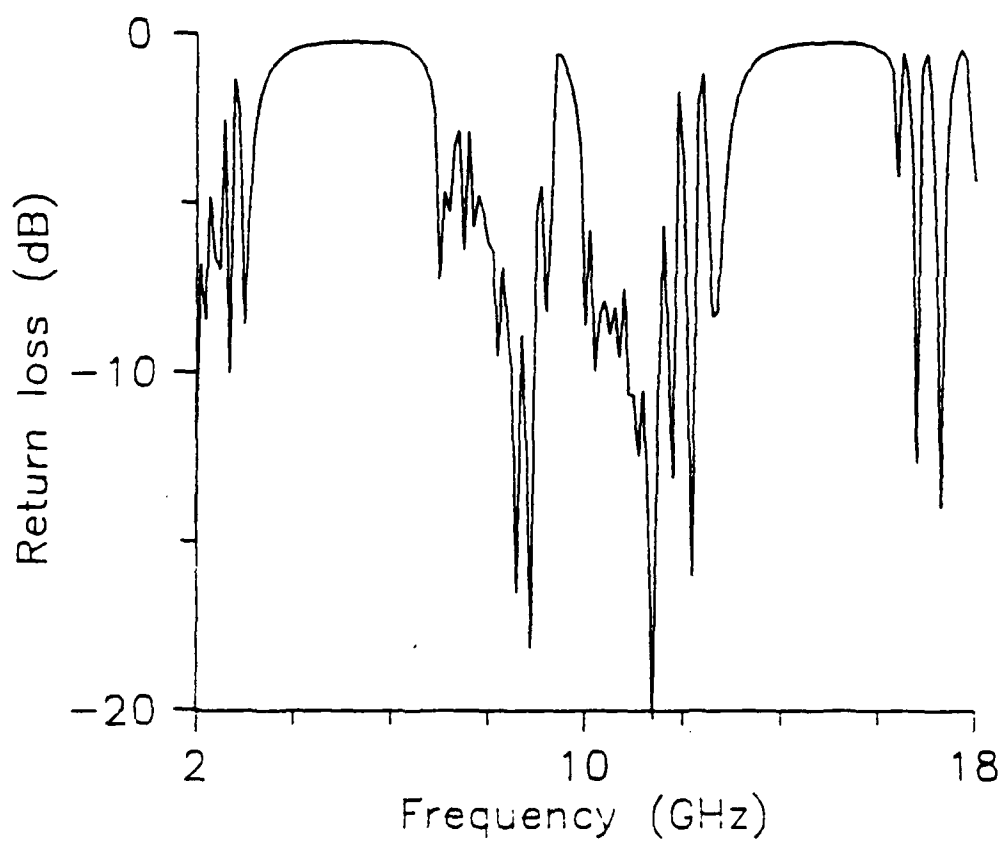
Figure 4.4   Calculated input return loss for a 17 patch
periodic antenna fabricated on Rogers Duroid
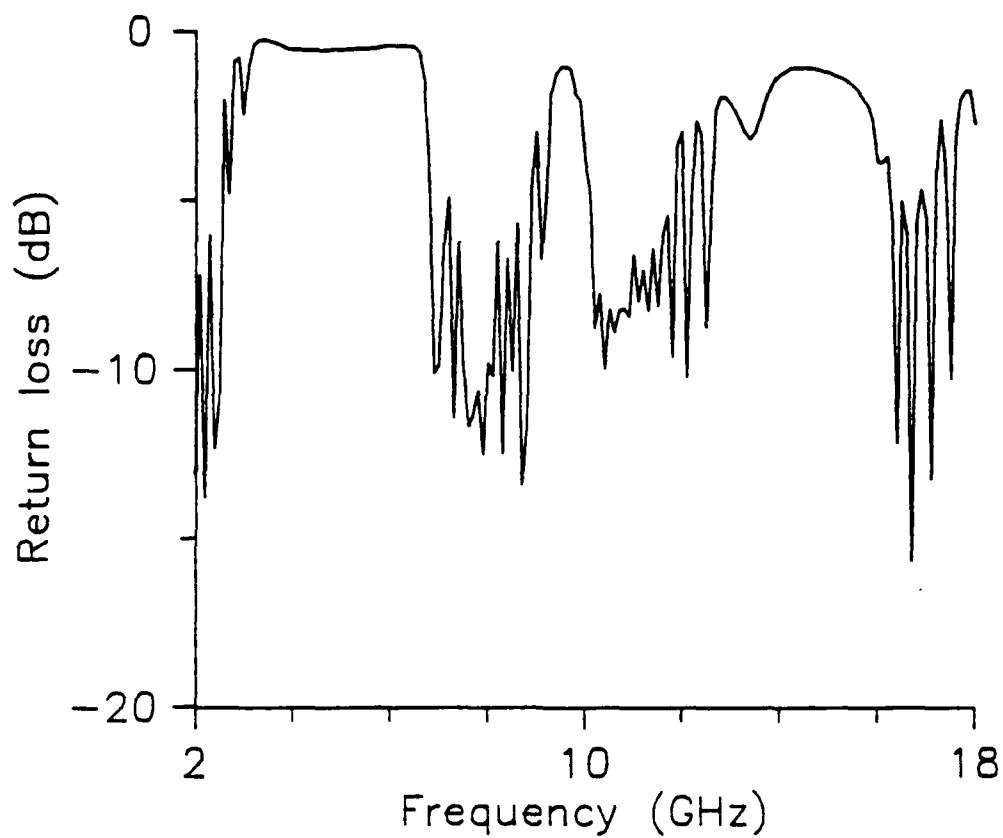6010.2 substrate (ε_r = 10.2, h=.635 mm).

Figure 4.5   Measured input return loss for a 17 patch
periodic antenna fabricated on Rogers Duroid
6010.2 substrate (ε_r=10.2, h=.635 mm).

discussed in the next Chapter. In addition, it was discovered that the agreement between the predicted and actual performance was poor, with the actual performance being much better than that predicted using the above approach. For this reason, it was determined that the empirical approach outlined on page 43 was the best choice for the circuit design.

As mentioned above, the low impedance of the patch elements causes the surface wave stop-band to be quite broad and generally causes the reflection properties of the structure to be poor. This may cause problems with oscillation at an unwanted frequency. To prevent these problems, it is necessary to terminate the gate of the device in a filter structure. The requirements on the filter are that it furnish a reactive load to the gate of the FET which falls into the output stability circle at the desired oscillation frequency. Also, at frequencies above and below the operating frequency, the reflection coefficient of the filter should move away from the stability circle, and therefore reduce the magnitude of the negative impedance at the drain. Since in this case, the reflection coefficient of the broad surface-wave stop-band traverses nearly the whole periphery of the Smith chart as the frequency is varied, the safest option is to adjust the gate filter so that no negative resistance is present at the drain of the FET over this whole frequency range, although this is not necessary in general.

The first approach to the gate filter was to use another periodic structure on the gate of the device, except with one-half the period of the leaky-wave antenna. This creates a stop-band at the frequency where it is desired to have oscillation, and pass-bands elsewhere, specifically at one half of this frequency. By making the structure long and the impedance steps small, it is possible to create a very narrow stop-band. In this case, the gate filter becomes the primary frequency selective element in the design.

The other alternative is to use a low-pass structure on the gate. In this case, the oscillation frequency is located within the stop-band of the pass filter, and the frequency of the surface-wave stop-band for the periodic antenna corresponds to the pass-band of the gate filter.

Both of the approaches described above were tried. The design frequencies for the prototype circuits were all 10 GHz. This frequency was chosen because of the ease of construction and the fact that test equipment at this frequency is readily available. The general circuit topography appears in Figure 4.6. In this circuit, as in all described in this dissertation, the FET used was a low cost, packaged version of the NEC 71083. The FET is operated in the self-biasing configuration, which allows the use of a single dc supply. In this case, the source is connected through a resistor to ground, which primarily determines the drain current. The gate is grounded, and the voltage applied to the drain then determines V_{ds}.

Figures 4.7 through 4.9 show the radiation patterns for three circuits. The results shown in Figure 4.7 are for a circuit with a 16 element patch array antenna and a 15 element band-stop filter on the gate, Figure 4.8 for a 12 element antenna and a 7 element band-stop filter on the gate, and in Figure 4.9 for a 17 element antenna and a 3 element low-pass filter on the gate. All of the radiation patterns were measured using a compact test range and a Narda x-band standard gain horn coupled to an Anritsu microwave power meter. The oscillation frequencies for the circuits were 9.66 GHz, 9.87 GHz, and 9.54 GHz, respectively. These values were all within 5% of the design frequency of 10 GHz.

The overall lengths of the circuits were 25, 17, and 20 cm respectively. In the circuits with the band-stop filters on the gates, the antenna comprised only slightly

+ V

Microstrip patch array

FET

low pass or
band stop filter
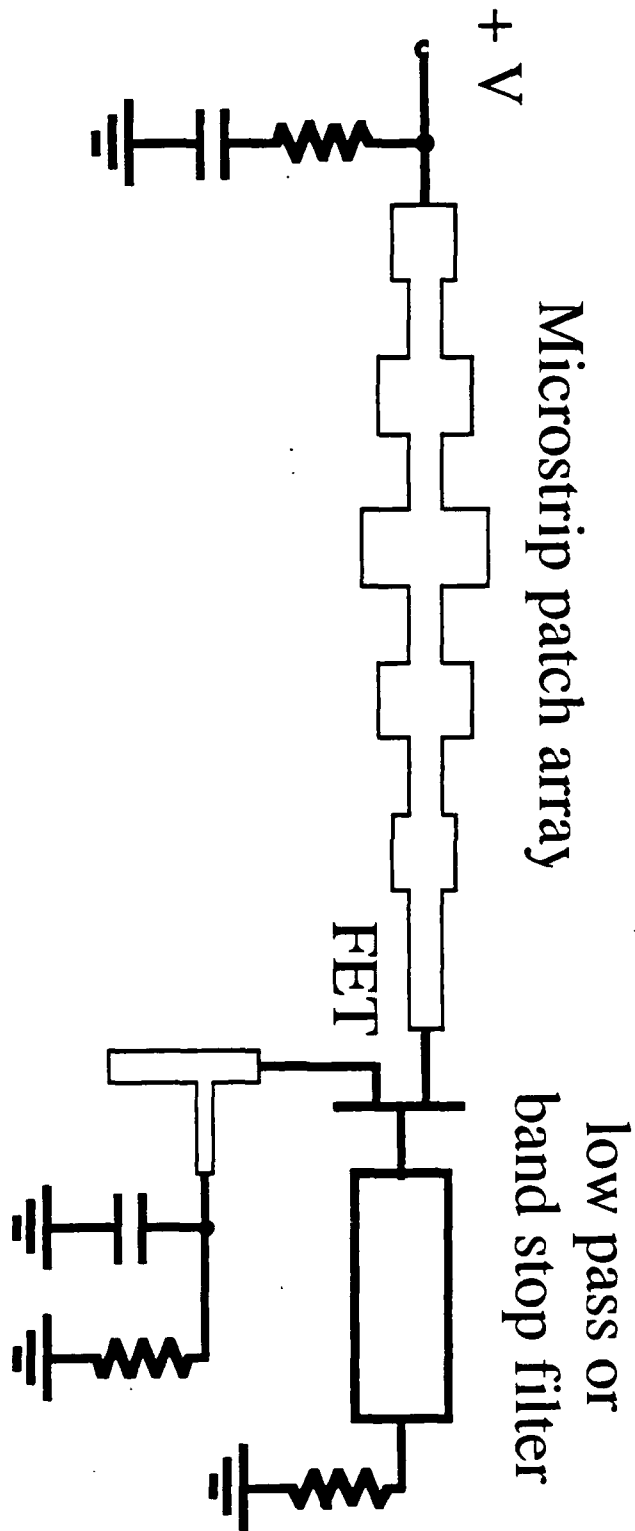
Figure 4.6.   Schematic diagram of single device oscillator circuit.

Figure 4.7   Radiation patterns for the single device
             oscillator circuit with a 16 element patch
             array and a 15 element band—stop filter
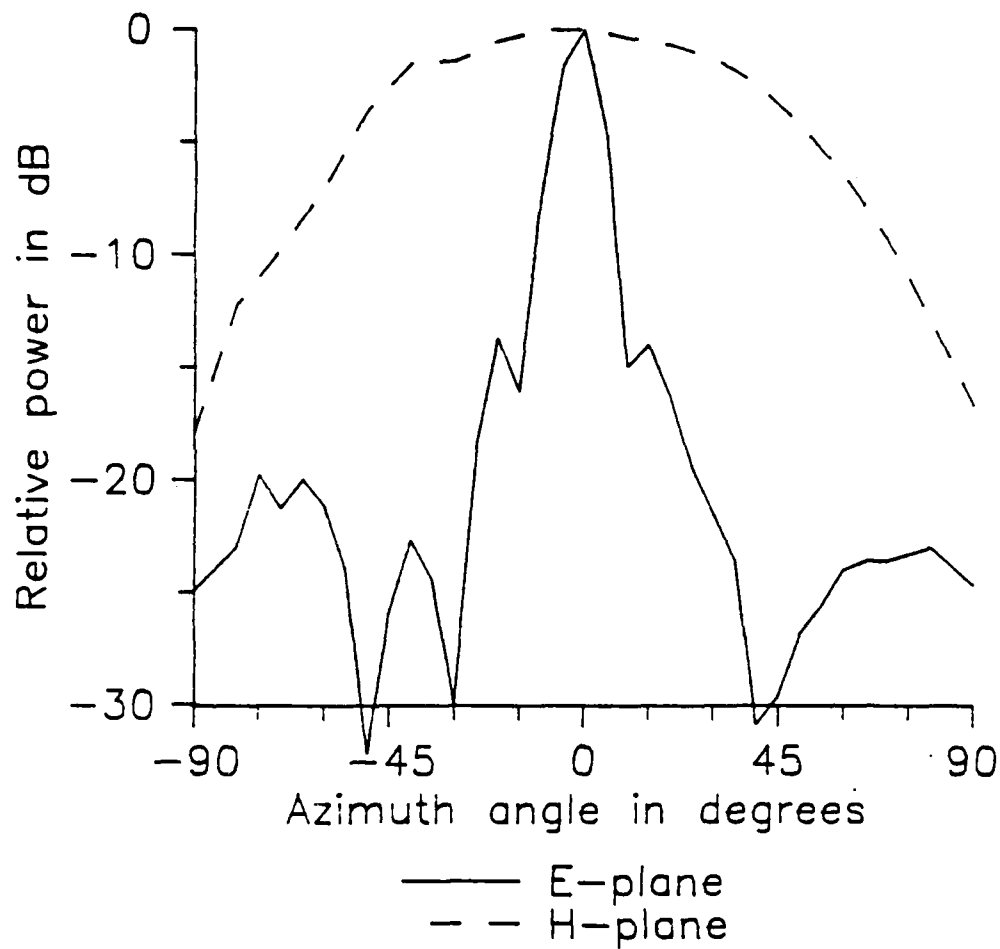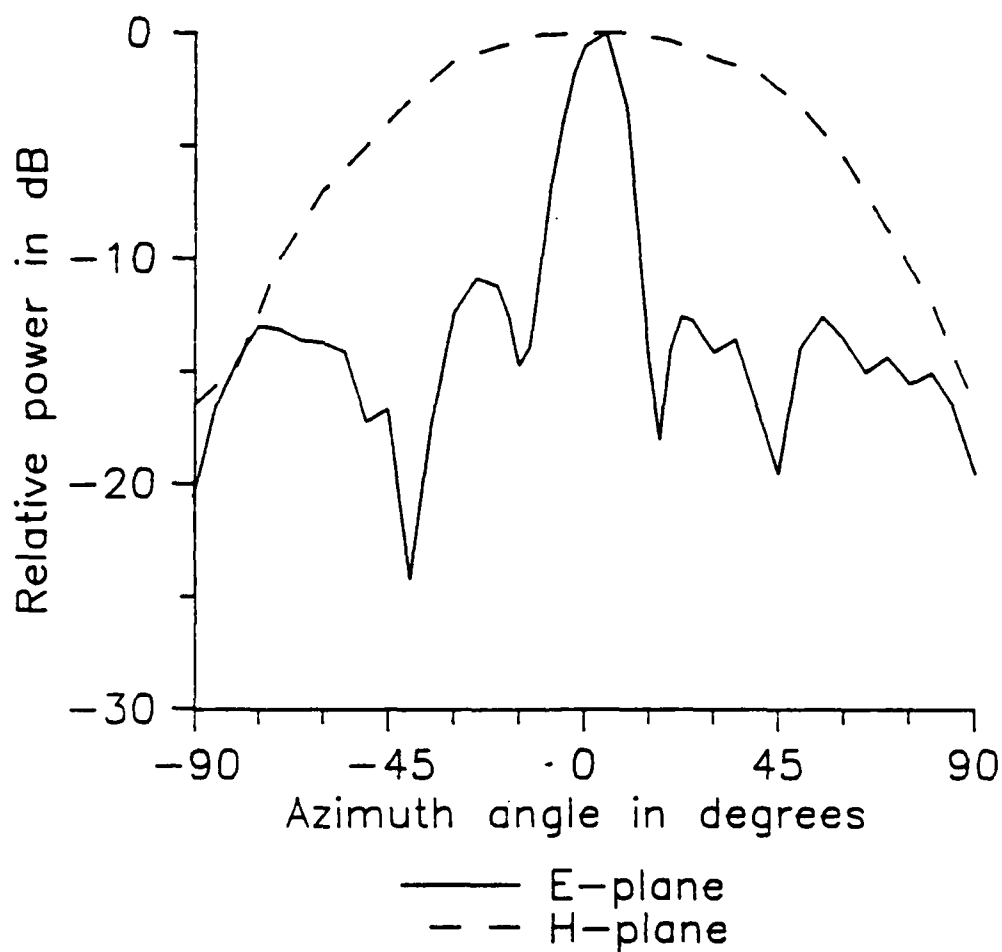   on the gate.

Figure 4.8   Radiation patterns for the single device
oscillator circuit with a 12 element patch
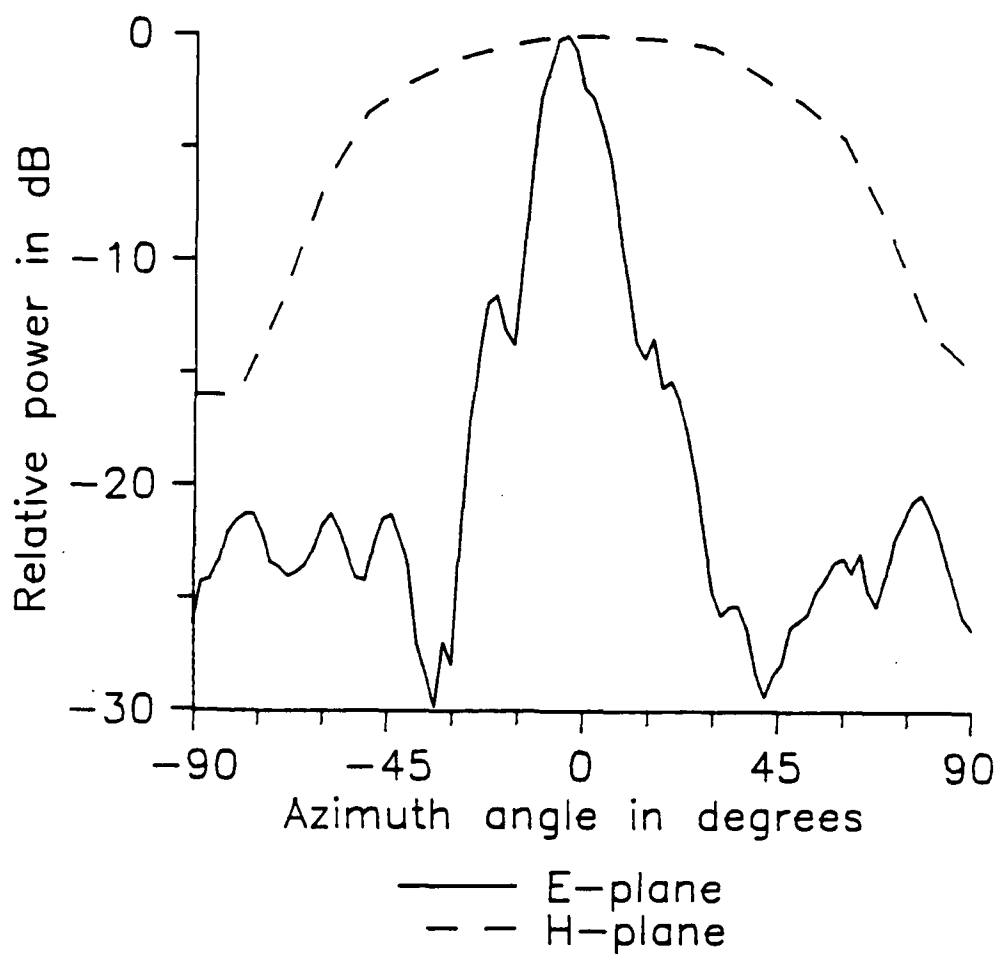array and a 7 element band—stop filter
on the gate.

Figure 4.9   Radiation patterns for the single device oscillator circuit with a 17 element patch array and a 3 element low-pass filter on the gate.

more than 50 % of the overall length of the circuit, while the circuit with the more compact low-pass filter on the gate had the antenna measuring more than 90% of its total length. A photograph of the latter circuit appears in Figure 4.10.

The tuning of the circuits was not difficult, indeed, oscillation took place immediately for each of the circuits tested. The main adjustment on the circuits was trimming of the source feedback stub. It was found early on that radiation from this microstrip open circuit could significantly affect the overall pattern for the oscillator. The circuit adjustment therefore amounted to trimming this stub so that the radiation was minimized while still maintaining oscillation at the desired frequency. Fortunately, the nature of the soft substrate is such that the copper metallization may be easily added and removed from the stub.

It is difficult to separate the oscillator circuits described here into separate generators and antennas for the purpose of determining their performance. For this reason we examine the performance of the circuit as a whole by defining the isotropic transmit gain, G_{iso}^T, as the ratio of power radiated in a particular direction to that due to an isotropic source radiating with a strength equal to that of the dc bias supply. This is exactly similar to the isotropic conversion loss defined in [5]. This quantity is determined by measuring the received power in the far field due to the oscillator at a given bias condition, and comparing the result with the received power due to a standard gain horn driven with a known excitation level. The test setup is shown schematically in Figure 4.11. We may write the following expressions for the two received powers, where all quantities are expressed in decibels:
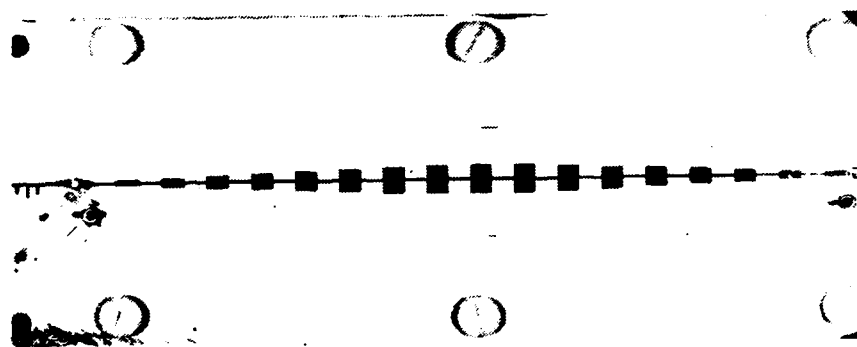
$$P_o = P_{dc} + G_{iso}^T + K$$

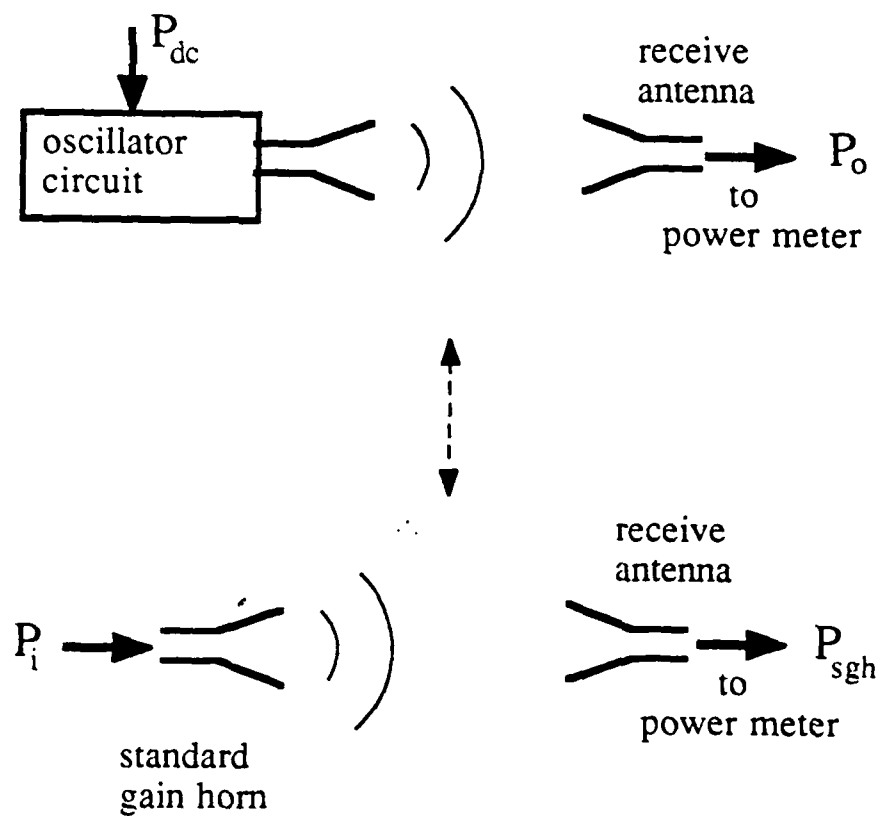Figure 4.10 Photograph of the oscillator circuit with the low-pass gate filter.

Figure 4.11. Schematic diagram of the test setup
for the determination of isotropic
transmit gain.

$$P_{sgh} = P_i + G_{sgh} + K$$

where P_o is the received power due to the oscillator, P_{dc} is the dc power used by the oscillator circuit, (computed by measuring the drain to source voltage V_{ds}, and multiplying by the drain current, I_d), P_{sgh} is the received power due to the standard gain horn, P_i is the power input to the standard gain horn, G_{sgh} is the gain of the horn, and K is a constant associated with the test setup which includes the path loss and the properties of the receiving antenna and the power meter. We take the difference of the two equations and re-arrange the terms to arrive at:

$$G_{iso}^{T} = P_o - P_{sgh} - P_{dc} + P_i + G_{sgh}$$

where all of the terms on the right hand side are known. The isotropic transmitter efficiency may be related to the effective radiated power (ERP) in decibels by:

$$ERP = G_{iso}^{T} + P_{dc}$$

The isotropic transmitter gain is therefore a measure of how well the circuit converts the input dc power and delivers it to a target. The measured G_{iso}^{T} for the three circuits described above are 7 dB, 2.5 dB and 9 dB, respectively.

The simple model of the FET given in Chapter Three indicated that the oscillation frequency and output power of the oscillator circuit may be varied by varying the gate voltage and thereby changing the value of the Schottky capacitor C_{gs}.

To determine the extent of the tuning range available and its linearity, the gate voltage was varied relative to the source and drain of the FET by leaving the gate grounded and varying the source resistance and supply voltage. The frequency and output power were measured using a Tektronix 492 AP spectrum analyzer using a horn antenna in the near field. This setup gives relative output power variations only. The broadest tuning range was given by the oscillator circuit with the low-pass filter on the gate, probably because of the lower Q of its gate circuit compared to the band-stop filter configuration. Tuning range and relative output power for the circuit with the low-pass gate filter is shown in Figure 4.12. The broad linear tuning range (~ 40 MHz) for the latter circuit indicate that this circuit is capable of good frequency modulation.
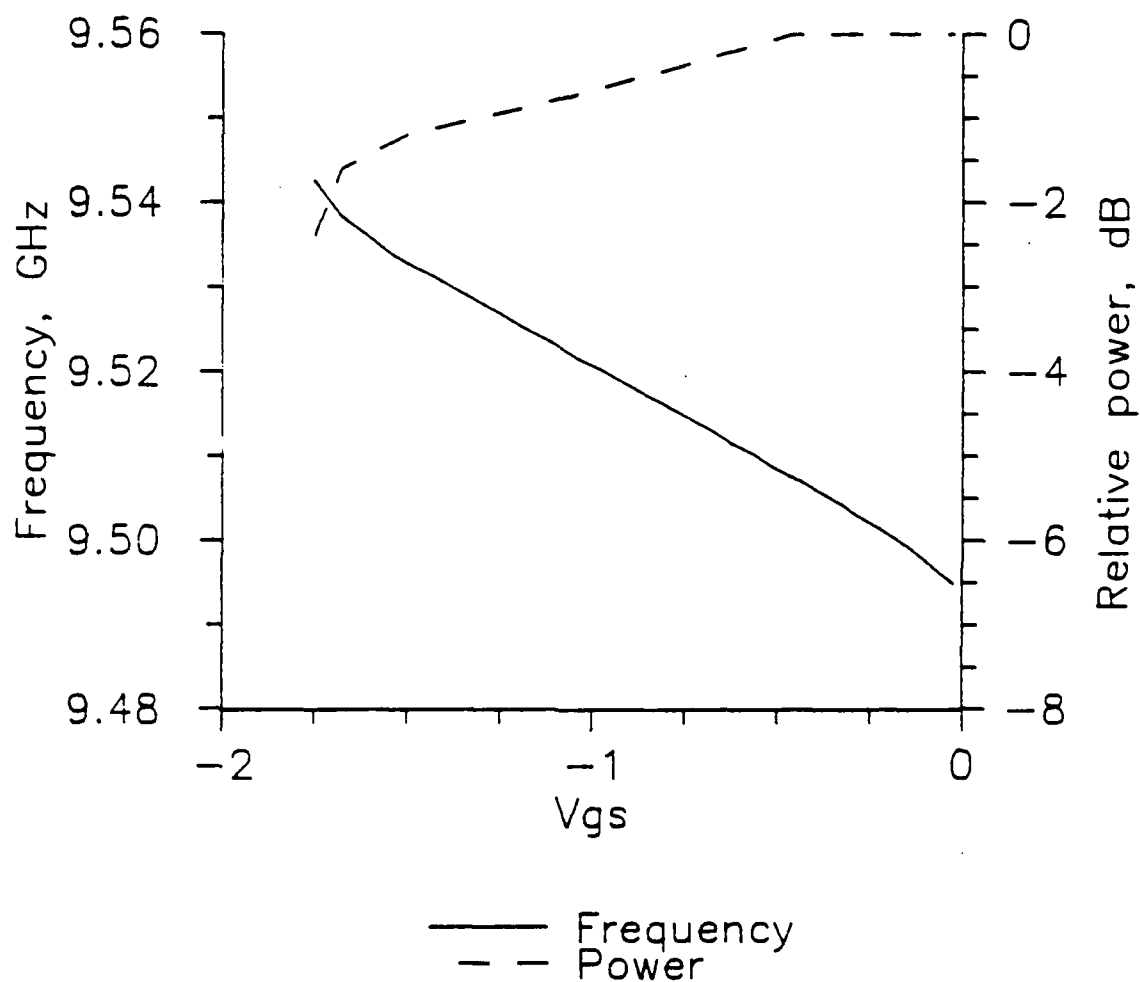
Figure 4.12 Tuning range and relative output power
for the oscillator with the low—pass gate
filter and 17 element antenna.

CHAPTER 5: THE DUAL DEVICE OSCILLATOR

The dual device oscillator is similar in principle to the single device oscillator described in the previous chapter, except that in this case the resonant antenna has two input ports to provide connections for two active negative resistance devices. The oscillator circuit is symmetrical, meaning that its operation can be analyzed in terms of even and odd modes of oscillation. By proper design of the antenna, the circuit may be forced to oscillate in one or the other of these modes. Operation in the odd mode, with the FETs oscillating 180 degrees out of phase is referred to here as push-pull. In this case, the output powers of the devices are added at the fundamental frequency. In the even mode, where the FETs oscillate in phase, the operation is referred to as push-push. In this case, the radiated power of the devices cancels at the fundamental frequency, but adds at the second harmonic. This is useful for generation of power at frequencies higher than may be easily achieved using one device.

The operation of the circuit in the manner described above is dependent on the structure of the microstrip antenna. The type of antenna which is used in our circuits is the coupled rampart line antenna.

The single rampart line antenna, which was first described by Hall [29], is shown in Figure 5.1 a). This antenna consists of straight sections of microstrip line connected by mitered bends. We use the planar waveguide model to illustrate the radiation mechanism of this structure; this is essentially the same technique as the cavity model used in the previous chapter for analysis of the microstrip patch radiator. Figure 5.1 b) shows the equivalent planar waveguide formed by placing magnetic walls along the edges of the microstrip line. $\vec{K}$ denotes the value of the equivalent magnetic current
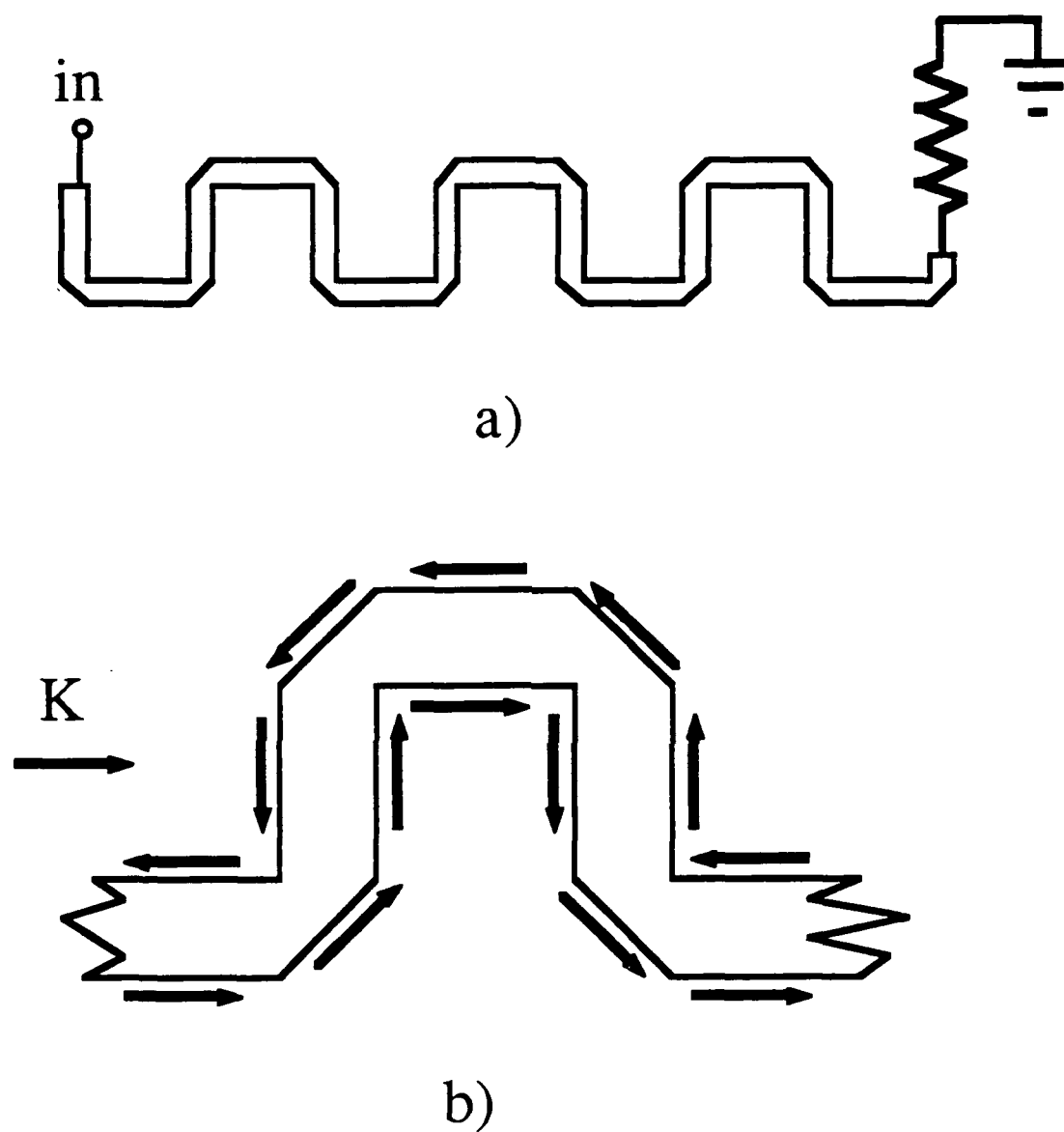
Figure 5.1. The microstrip rampart line antenna: a) plan view; b) planar
waveguide model showing equivalent magnetic currents.

flowing on the magnetic walls required to support the TEM fields of the guide. The magnetic currents flow in opposite directions along the edges of the microstrip. Since the line is generally much narrower than the free space wavelength, this model indicates that the radiation due to the straight sections of microstrip will be nearly zero for a range of frequencies in the vicinity of broadside, with a null at exactly broadside. For the mitered bends, however, the magnetic current on the outside is unopposed, so that there will be net radiation from this region. If the lengths of transmission line between the mitered bends is adjusted properly, the overall radiation from the structure may be varied among many options [29]. In particular, if the section is $\lambda_m/4$, the radiation is polarized with the E-plane perpendicular to the axis of the antenna, while if the section length is $\lambda_m/2$, the radiation is polarized parallel to the axis of the antenna.

The coupled rampart line antenna is shown in Figure 5.2. The circuit is formed by placing two rampart line antennas side by side so that the adjacent sections are coupled as shown in the figure. Neglecting for the moment the coupling between the antennas, we may analyze this structure using the same technique given in the previous paragraph. For our approximate analysis, we assume that the voltage at all corners are equal, and we calculate the contribution of the fringing field from each of the bends in a single cell to the total field at broadside.

First we perform the analysis for the case of the straight line sections with length $\lambda_m/4$ with even and odd excitation. In the broadside direction, the fields due to each of the mitered bends for one cell of the periodic structure are shown in Figure 5.3. We see that the total field for the antenna is zero for the even excitation, and it is polarized perpendicularly to the axis of the antenna for the odd excitation. In the even case, the

Coupled Section
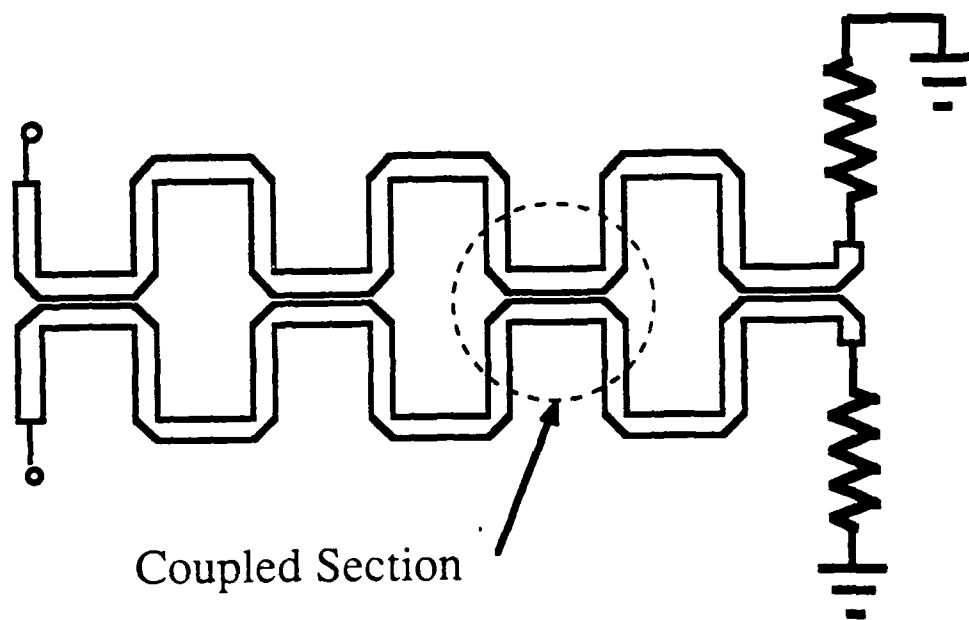
Figure 5.2   The coupled microstrip rampart line antenna.

3 7

4 8

y

x

1 5

2 6

$\lambda/4$
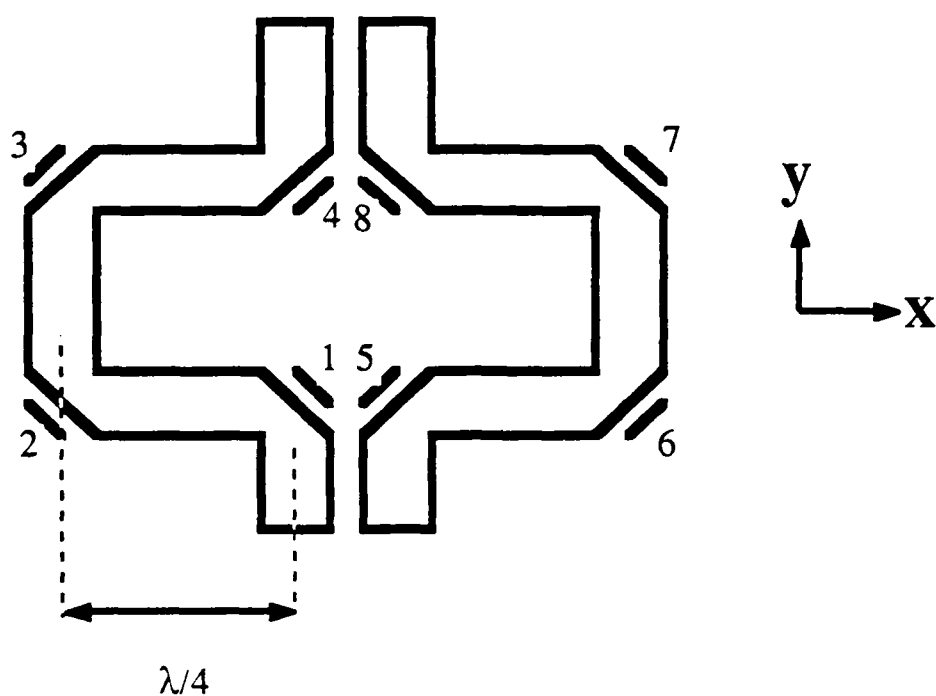
Figure 5.3 The coupled microstrip rampart line antenna with odd excitation.

bend no.	even mode	odd mode
1	$-\hat{x}+\hat{y}$	$-\hat{x}+\hat{y}$
2	$j\hat{x}-j\hat{y}$	$j\hat{x}-j\hat{y}$
3	$\hat{x}+\hat{y}$	$\hat{x}+\hat{y}$
4	$-j\hat{x}-j\hat{y}$	$-j\hat{x}-j\hat{y}$
5	$-\hat{x}-\hat{y}$	$\hat{x}+\hat{y}$
6	$j\hat{x}+j\hat{y}$	$-j\hat{x}-j\hat{y}$
7	$\hat{x}-\hat{y}$	$-\hat{x}+\hat{y}$
8	$-j\hat{x}+j\hat{y}$	$j\hat{x}-j\hat{y}$
total	0	$(4-4j)\hat{y}$

Table 5.1 Net magnetic current for the antenna of Figure 5.3.

radiation is null in the broadside direction. Note that we assume the length of the mitered bends to be negligible in this analysis.

Figure 5.4 shows a similar antenna, except that the distance between the mitered bends is now $\lambda_m/2$. In this case, we see that the even mode will radiate to broadside, while the odd mode is cancelled.

To determine the implications of the above analysis, we may imagine a coupled rampart line antenna where the lengths of the straight sections are $\lambda_m/4$ at a given frequency f_0. If we apply a signal to the inputs of this antenna which consists of a fundamental component at f_0 plus a second harmonic at $2 f_0$, then the odd mode portion at the fundamental will be radiated to broadside polarized perpendicular to the axis of the antenna, while the even mode portion of the second harmonic component will be radiated in the broadside direction with the opposite polarization. This means that if we can cause two FETs connected to the inputs of the antenna to oscillate in the odd mode, the signal will be radiated in the broadside direction, polarized perpendicular to the axis of the antenna, while if the FETs are caused to radiate in the even mode with sufficient second harmonic, then the second harmonic will be radiated, polarized parallel to the antenna axis, and the fundamental suppressed.

One way to cause the FETs to oscillate in the desired mode is to cause the rampart line antenna, which is a periodic structure, to exhibit stop-bands in the desired mode, and to behave as a termination in the opposite mode. In this way, feedback is applied to the FETs only in the desired mode, which will allow oscillation to occur in this mode only. The way to achieve this is by adjustment of the coupled sections, which we now examine.
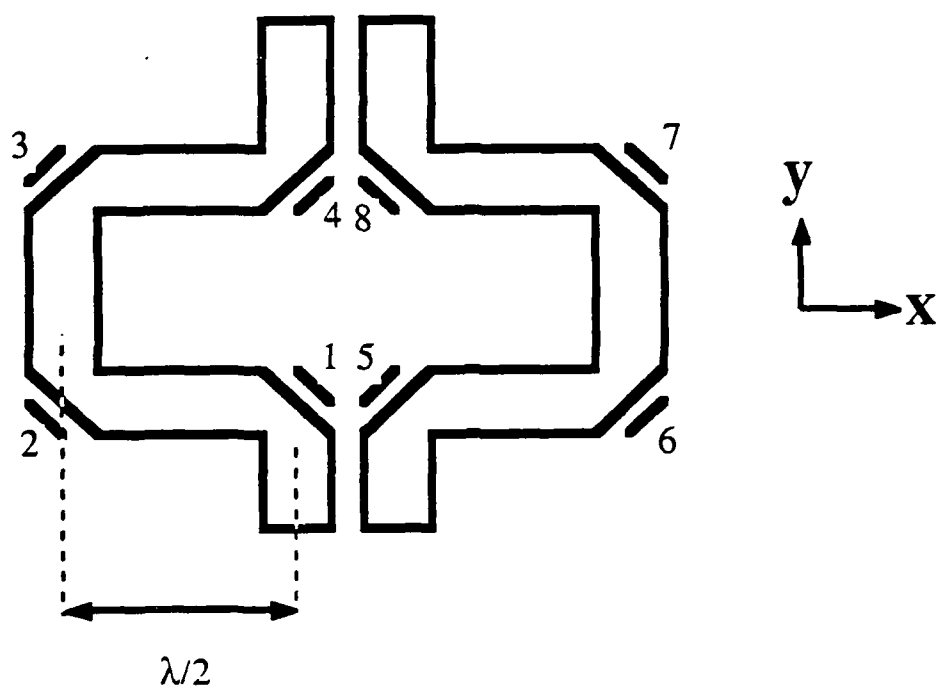
Figure 5.4 The coupled microstrip rampart line antenna with even excitation.

bend no.	even mode	odd mode
1	$-\hat{x}+\hat{y}$	$-\hat{x}+\hat{y}$
2	$-\hat{x}+\hat{y}$	$-\hat{x}+\hat{y}$
3	$-\hat{x}-\hat{y}$	$-\hat{x}-\hat{y}$
4	$-\hat{x}-\hat{y}$	$-\hat{x}-\hat{y}$
5	$-\hat{x}-\hat{y}$	$+\hat{x}+\hat{y}$
6	$-\hat{x}-\hat{y}$	$+\hat{x}+\hat{y}$
7	$-\hat{x}+\hat{y}$	$+\hat{x}-\hat{y}$
8	$-\hat{x}+\hat{y}$	$+\hat{x}-\hat{y}$
total	$-8\hat{x}$	0

Table 5.2 Net magnetic current for the antenna of Figure 5.4.

A cross-sectional view of a pair of coupled microstrip lines appears in Figure 5.5, where the electric field lines are shown for the even and odd mode cases. In the even mode case, the voltage waves on the lines are in phase. In this case, the field lines occupy more free space. Therefore, the fringing capacitance of the individual lines is lowered and the inductance is increased, causing the characteristic impedance for this condition to be greater than that for the single microstrip line with the same dimensions. In the odd mode, the field lines are more concentrated in the dielectric, and hence the fringing capacitance is increased, while the inductance is lowered. In this case, then, the characteristic impedance of the structure is lowered relative to the single strip case. The characteristic impedance for the even mode case is denoted by Z_{0e}, while that for the odd mode case is denoted Z_{0o}. In addition to the effect on the impedance of the coupled section, the coupling between the lines has a second order effect on the propagation constant which we do not consider here.

In order to calculate accurate values for Z_{0e} and Z_{0o}, it is necessary to examine the detailed behavior of the fields. This may be done using quasi-static techniques for low frequencies as in [30]. For a more accurate analysis, full wave methods must be employed [31]. The calculations of even and odd mode impedance used in this paper were performed using the Linecalc™ transmission line calculator program available from EEsof, Inc. of Westlake Village, CA. Their models are taken from the closed form expressions given in [32], which are based on full wave techniques.

For a given substrate thickness and dielectric constant, the characteristics of the coupled section may be specified by any one of the following pairs of constants: the width and spacing of the lines, the even and odd mode impedances, Z_{0e} and Z_{0o}, and the coupling coefficient C and characteristic impedance Z_0. The latter two constants are:
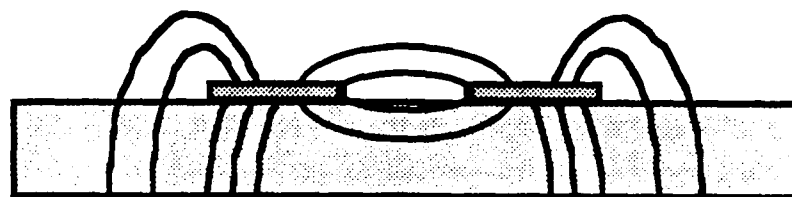
a)
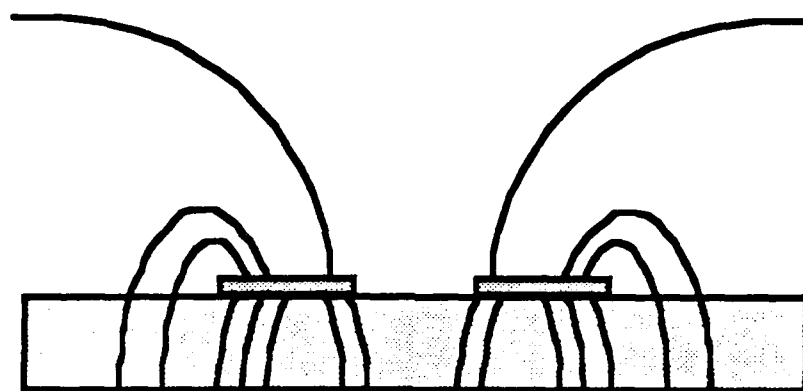
b)

Figure 5.5   Field distribtuion for a pair of coupled microstrip lines:
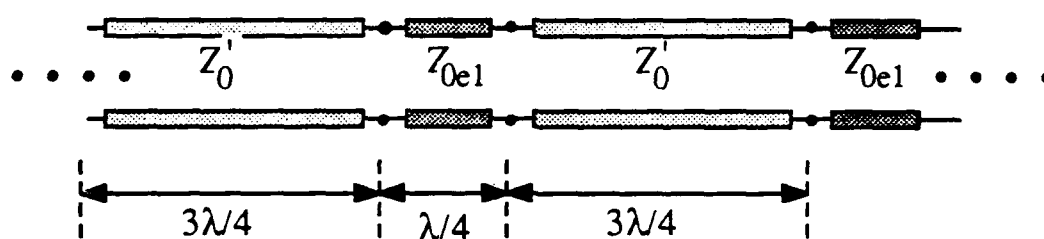a) odd mode, b) even mode.

$$C = \frac{Z_{0o} - Z_{0e}}{Z_{0o} + Z_{0e}} \qquad \text{and} \qquad Z_0 = \sqrt{Z_{0e} Z_{0o}}$$

The definitions for the latter two constants come from the analysis of the coupled quarter-wavelength microstrip lines as a four port device: When all of the ports are terminated with an impedance of Z_0, and a one volt excitation is applied at one of the ports will cause a voltage of magnitude C to appear at the adjacent port.

The even and odd mode equivalent circuits of the coupled rampart line antenna appear in Figure 5.6. In this figure, the impedance of the uncoupled sections is labeled Z_0', to distinguish it from the characteristic impedance of the coupled sections defined above. It is now apparent that if we construct the coupled sections so that $Z_{0e} = Z_0'$ and $Z_{0o} < Z_0'$, then the stop-bands will appear in the odd mode only, whereas if $Z_{0o} = Z_0'$ and $Z_{0e} > Z_0'$ obtains, the stop-bands will occur only in the even mode. Also, from the example of Figure 2.4, we see that in this case, there will be a leaky wave stop-band.

The analysis of this periodic structure is less complicated than that of the periodic patch array described in the previous chapter. Here the leaky-wave stop-band is due solely to the impedance variations along the line, and not to the relatively complicated behavior of the junction parasitics as with the patch array. Also the radiation occurs from the mitered bends, which depend only slightly on the impedance of the coupled sections. In the patch array, the radiation resistance of each step discontinuity is strongly dependent on the impedance of the sections.

The radiation from the structure may be analyzed using the planar waveguide approach as mentioned above, except now we include the effects of the coupled sections on the amplitudes of the magnetic currents at each mitered bend. Since the magnetic
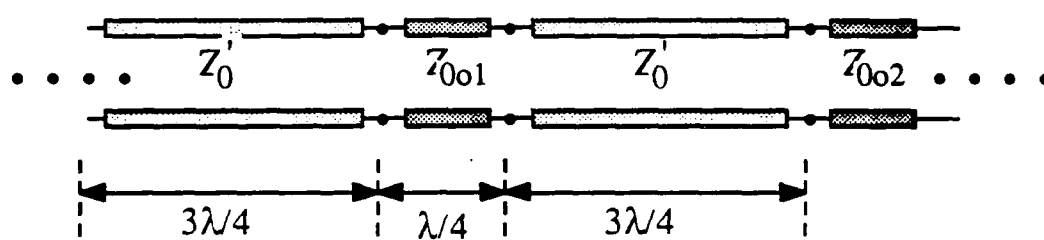
Figure 5.6. Equivalent circuits for the coupled rampart line antenna:
a) even mode, b) odd mode.

currents at each bend are proportional to the voltages at these points, we need only determine the voltages along the antenna. Once again, in this analysis we neglect the radiation from the miters when we establish the voltage along the antenna. The validity of this approach was determined by creating equivalent models for the antenna with and without these equivalent resistances using Touchstone™. The results of this analysis indicated that the voltages at the bends were only slightly affected by the inclusion of these resistances, with the maximum error about five percent at the first node and below two percent for the remainder of the nodes.

Figure 5.7 shows one half of the antenna connected to a source and a termination resistor, along with an indexing system for the mitered bends. Here we identify each mitered bend with a pair of indices, the first indicating a particular unit cell for the periodic antenna, and the second running from 1 to 4 to indicate one of the four corners in that cell. The voltages at each bend are determined by making an imaginary cut at that point and replacing the circuit on both sides of the cut with its Thevenin equivalent. The equivalent circuit used to determine the voltage at the $(n,2)$ bend, for example is shown in Figure 5.8.

The Thevenin equivalent impedance Z_{TH} and voltage V_{TH} for a lossless transmission line of length θ with impedance Z_0 connected to generator with voltage V_S and internal impedance Z_S are given by

$$Z_{TH} = Z_0 \frac{jZ_0\tan\theta + Z_S}{jZ_S\tan\theta + Z_0} \quad \text{and} \quad V_{TH} = \frac{-jZ_0V_S}{Z_S\sin\theta - jZ_0\cos\theta}$$
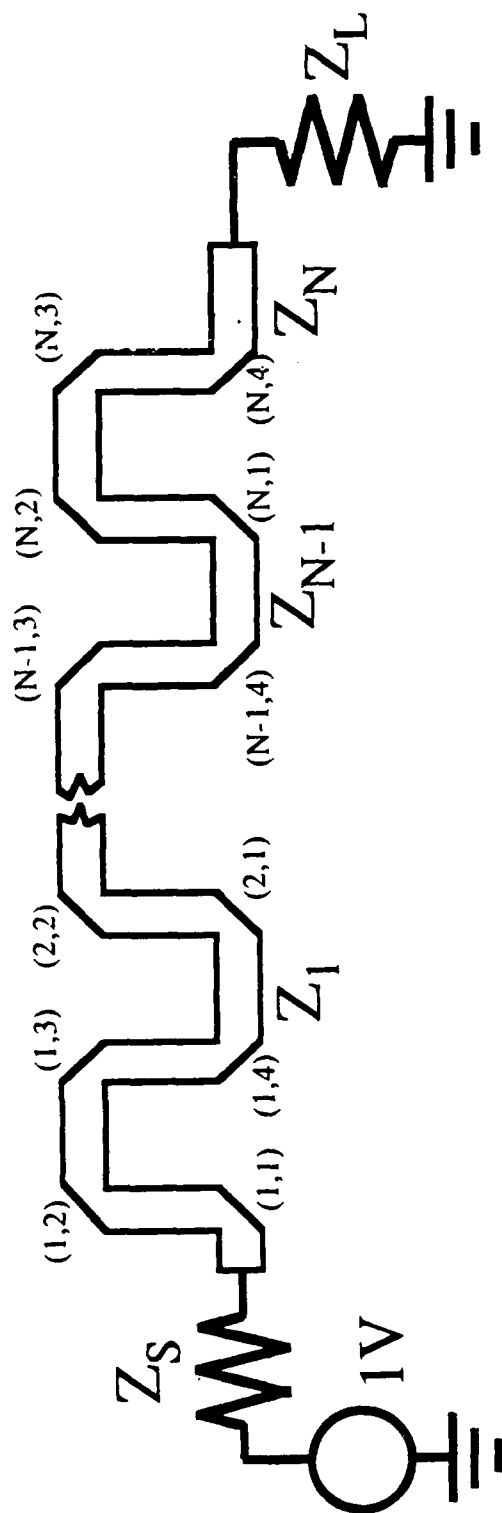
Figure 5.7 The equivalent circuit for the rampart line antenna with the indexing system for the mitered bends.
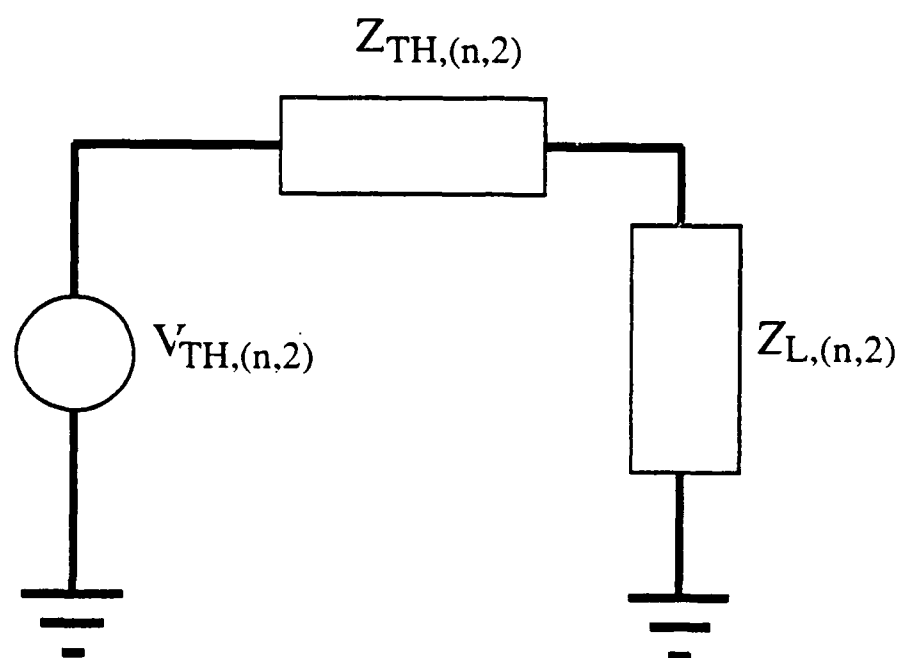
Figure 5.8. Equivalent circuit for the determination of the voltage at node (n,2).

which reduce to

$$Z_{TH} = \frac{Z_0^2}{Z_S} \quad \text{and} \quad V_{TH} = -j\frac{Z_0}{Z_S} V_S \qquad \text{when } \theta = \pi/2$$

and

$$Z_{TH} = Z_S \quad \text{and} \quad V_{TH} = - V_S \qquad \text{when } \theta = \pi.$$

in this analysis the electrical length of the bend is absorbed into θ. The evaluation of the Thevenin equivalents proceeds by starting at the source end for the various generator impedances and voltages and at the termination of the antenna for the load impedances. When the equivalent impedances are all expressed in terms of the coupled sections, expressions for the voltages at the various nodes may be derived. For the case with $\theta = \pi/2$, we get

$$V_{n,1} = -j\, D^{-1}\, Z_T \prod_{i=1}^{n-1} Z_i$$

$$V_{n,2} = -D^{-1} \prod_{i=1}^{N} Z_i^2 \prod_{i=1}^{n-1} Z_i^{-1}$$

$$V_{n,3} = -V_{n,1}$$

$$V_{n,4} = -V_{n,2}$$

where Z_i is the odd-mode impedance of the ith coupled section, Z_T is the termination impedance, Z_S is the source impedance, N is the total number of coupled sections, j is the square root of -1, and

$$D = Z_T Z_S + \prod_{i=1}^{N} Z_i^2 \quad .$$

All impedances are normalized to the impedance of the uncoupled sections. For the case with $\theta = \pi$, we get

$$V_{n,m} = -\frac{Z_T}{Z_T + Z_S} \qquad \text{for } m = 1,3$$

and

$$V_{n,m} = \frac{Z_T}{Z_T + Z_S} \qquad \text{for } m = 2,4$$

The simple expressions in this case arise from the fact that the leaky-wave stop-band has now disappeared.

The antenna performance was determined using the above expressions by assuming the magnetic current at each miter could be modeled as an infinitesimal dipole. A computer program was written to calculate the pattern for the antenna given the values of the coupling impedances.

From the point of view of the antenna as a band-stop filter, the design is also much less difficult than the periodic patch array. Since the antenna may be well modeled by using sections of ideal transmission line, the synthesis techniques for band-stop filter design given Park, et. al. [33] may be employed. However, this type of filter design is not quite appropriate for our problem, since the resulting filter may be over-specified.

In the case of our circuit, the filter properties of the antenna are not critical, and a "cut and try" approach using the CAD tools is more appropriate. Using Touchstone™, the return loss required of the antenna for optimal oscillator performance is determined as outlined in Chapter Three. The antenna is the modeled as a concatenation of quarter-wave sections of ideal transmission line in the desired operating mode, and as a resistive termination in the opposite mode. By varying the impedance of every fourth section of line, the necessary VSWR is realized. When the final design is begun, the ideal sections of line are replaced with the microstrip equivalents connected by the mitered bends.

To handle the design of the dual device circuit using Touchstone™, the even and odd equivalent circuits must be separately modeled. This is accomplished by placing resistors in the circuit model at nodes which lie on the axis of symmetry of the circuit. In this way, assigning the value $r = 0$ to these resistors places the circuit in the odd mode, while assigning a large value, such as $r = 10^9$ places the analysis in the even mode.

The nature of the coupled rampart line antenna is such that the surface-wave stop-band is not nearly as broad as for the periodic patch array, hence the design of the gate filter for the dual device oscillator is more relaxed. However, another requirement in this case is that the circuit not oscillate in the undesired mode. It was discovered that the use of a simple microstrip stub on the gate of the FETs worked well. In the case of the circuit designed to oscillate in the odd mode, for example, the gates of the FETs may be connected together using a section of microstrip line.approximately one half wavelength long. To prevent oscillations in the even mode, resistor is attached to ground at the mid point of the line. This does not affect odd mode performance, since this point is virtual ground in that case.

The dual device oscillator circuits were fabricated on Rogers Duroid 5880 substrate material with a relative dielectric constant of 2.2 and a thickness of .51 mm. The design frequency for the prototype circuits was 10 GHz. The lower dielectric constant material was used in this case to ease the construction of the coupled sections, which would require difficult widths and spacings using high dielectric constant material. This material also caused the circuits to become larger and further ease the fabrication difficulties.

A schematic diagram for the dual device oscillator circuit appears in Figure 5.9. Both the push-pull and the push-push oscillators used the same basic layout, with the dimensions of the coupled sections being the main difference. In both types of oscillators, a nine coupled section antenna was used, which measured approximately 10 cm in length.

For the push-pull oscillator, the odd mode impedances of the coupled sections ranged from 35 ohms in the center of the array to 42 ohms for the end sections. This corresponds to width = 74.7 mils and spacing = 7.3 mils for the centermost section and width = 69.4 mils and spacing = 27.1 mils for the end sections.

Radiation patterns for the push-pull oscillator appear in Figure 5.10 for the H-plane and Figure 5.11 for the E-plane, along with the predicted patterns given by the above analysis. The agreement between predicted and observed patterns for the H-plane results is reasonable, and suggests that parasitic radiation from the additional circuitry is only a minor factor in the overall pattern from the oscillator. The poor agreement between the predicted and observed data for the E-plane is not unexpected, since the array is much narrower along this axis, and hence the result depends more on the element pattern here. Interestingly, our predictions for the cross-polarized component
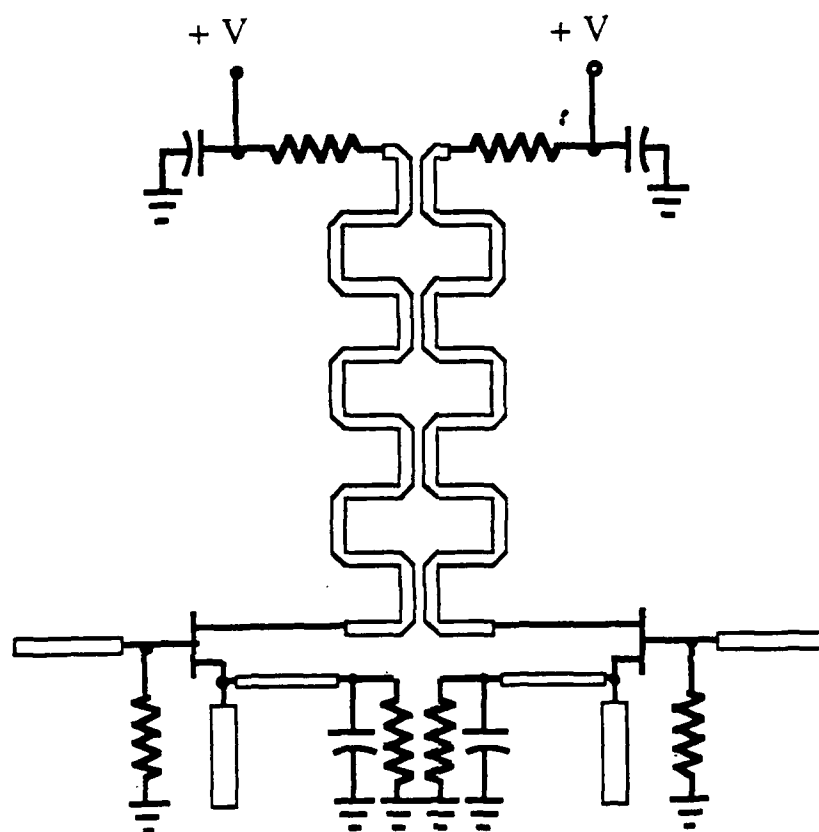
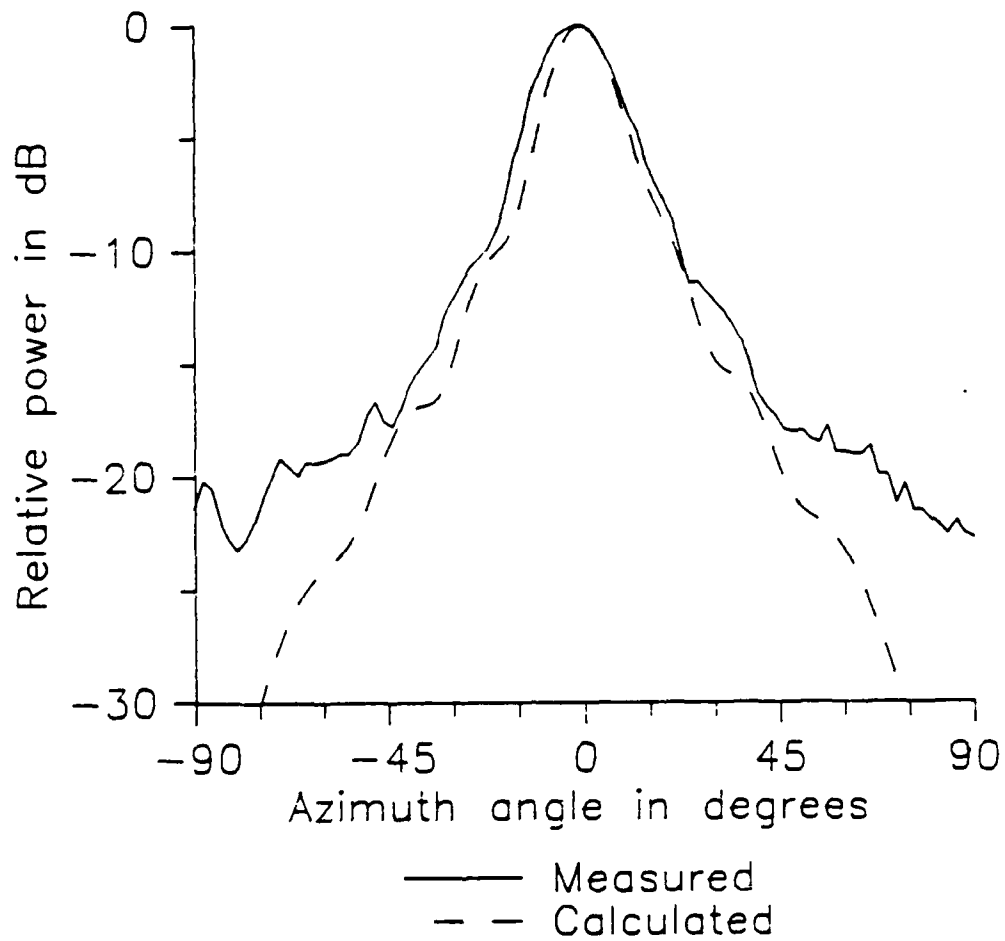Figure 5.9. A schematic diagram of the dual device oscillator circuit.

Figure 5.10 Calculated and measured H—plane patterns
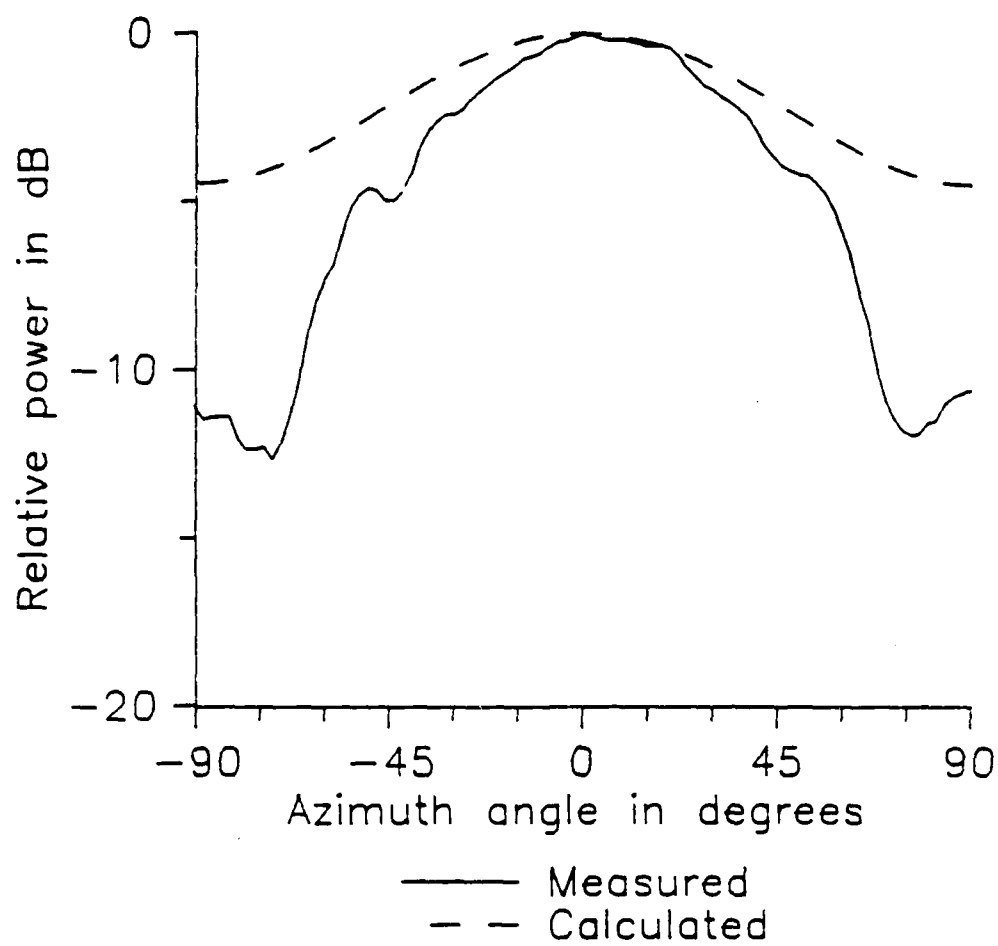for the push—pull oscillator.

Figure 5.11 Calculated and measured E–plane patterns
for the push–pull oscillator.

were much larger than the actual measured results. The model predicted maximum E-plane cross-polarization lobes to occur at azimuth angles of about ± 40 degrees from broadside about 9 dB below the main lobe, while the measured results were better than 20 dB down. It should be remembered, in this respect, that we only expect our predictions to be good in the vicinity of broadside.

It is difficult to determine the power combining efficiency for this structure, since we cannot construct any single element circuit with which to compare. One approach is to compare the power in the main beam with that due to the single device oscillator from before. In this case, we calculate a 140% power combining efficiency. Since the circuits are quite different, this may not be a valid comparison, especially since the single device circuit used for comparison was the best performer of the three single device circuits.

The push-push oscillator has been used for quite some time in the microwave industry, primarily using bipolar transistors [34]. It is attractive for that application since it allows the superior low noise performance of bipolar transistors to be extended to frequencies above x-band. These oscillators generally use varactor diodes, which greatly enhance the second harmonic generation. In our case we advocate the use of FETs in the push-push mode in quasi-optical fashion for the generation of microwave power at frequencies above that normally associated with these types of circuits.

A push-push oscillator was also constructed, in a similar fashion to that of the push-pull described above. In this case, for a typical nine element antenna, the even mode impedance of the centermost coupled section was 64 ohms while for the end sections it was 55 ohms. This corresponds to width = 42 mils and spacing = 10.5

mils for the centermost section and width = 56.7 mils and spacing = 50 mils for the end sections.

The circuit oscillated at 9.85 GHz, so that the desired output was observed at 19.7 GHz. The isotropic conversion efficiency and ERP in the broadside direction for the push-push circuit were measured for the second harmonic, and the results plotted in Figure 5.12. The radiation patterns for the fundamental and second harmonic are plotted in Figures 5.13 and 5.14.

It may be seen from these figures that the fundamental power output from the push-push oscillator is larger that that of the second harmonic. This is a problem common to push-push oscillators. In standard designs, a filter is added to the output of the oscillator to eliminate the fundamental. In the quasi-optical approach, a dielectric grating may be used to separate the fundamental and second harmonic waves.
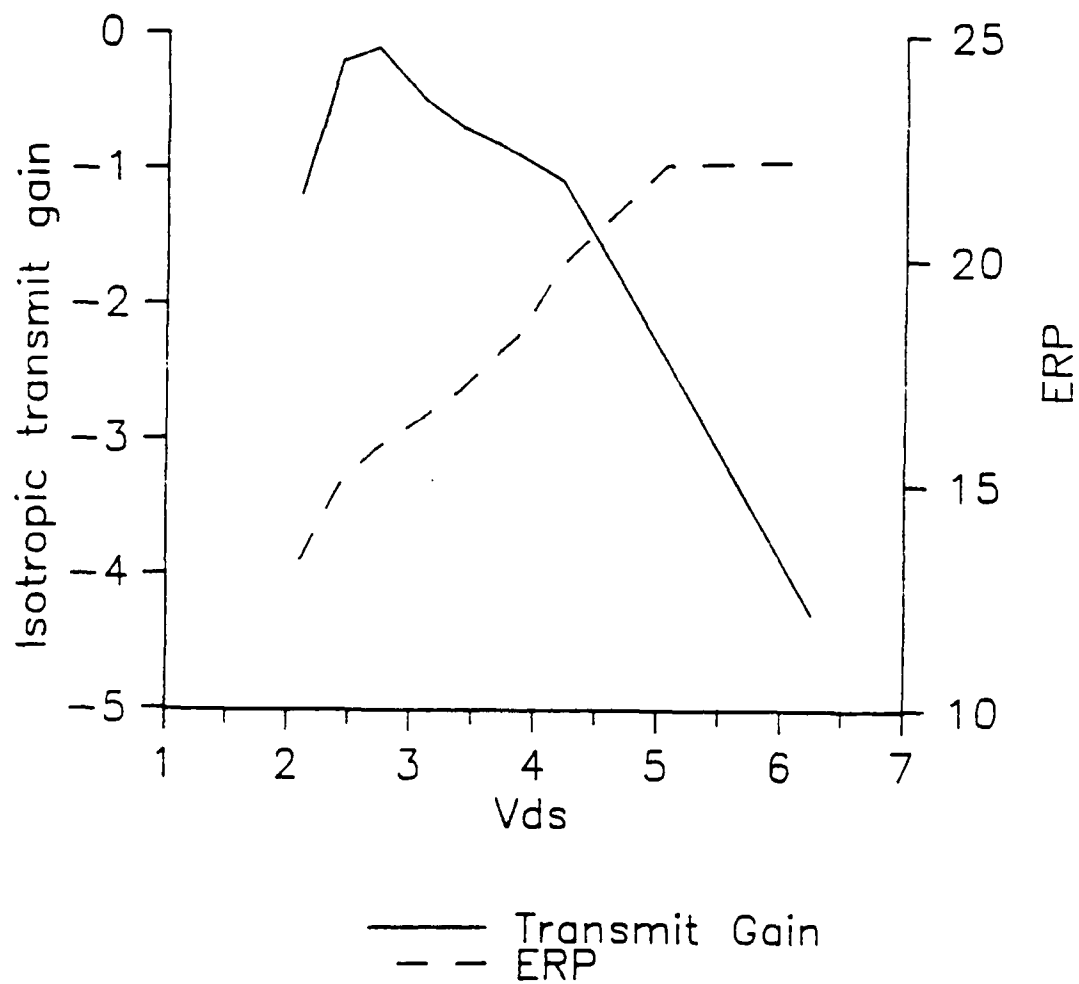
Figure 5.12 G^T_{iso} and ERP for the push—push oscillator.
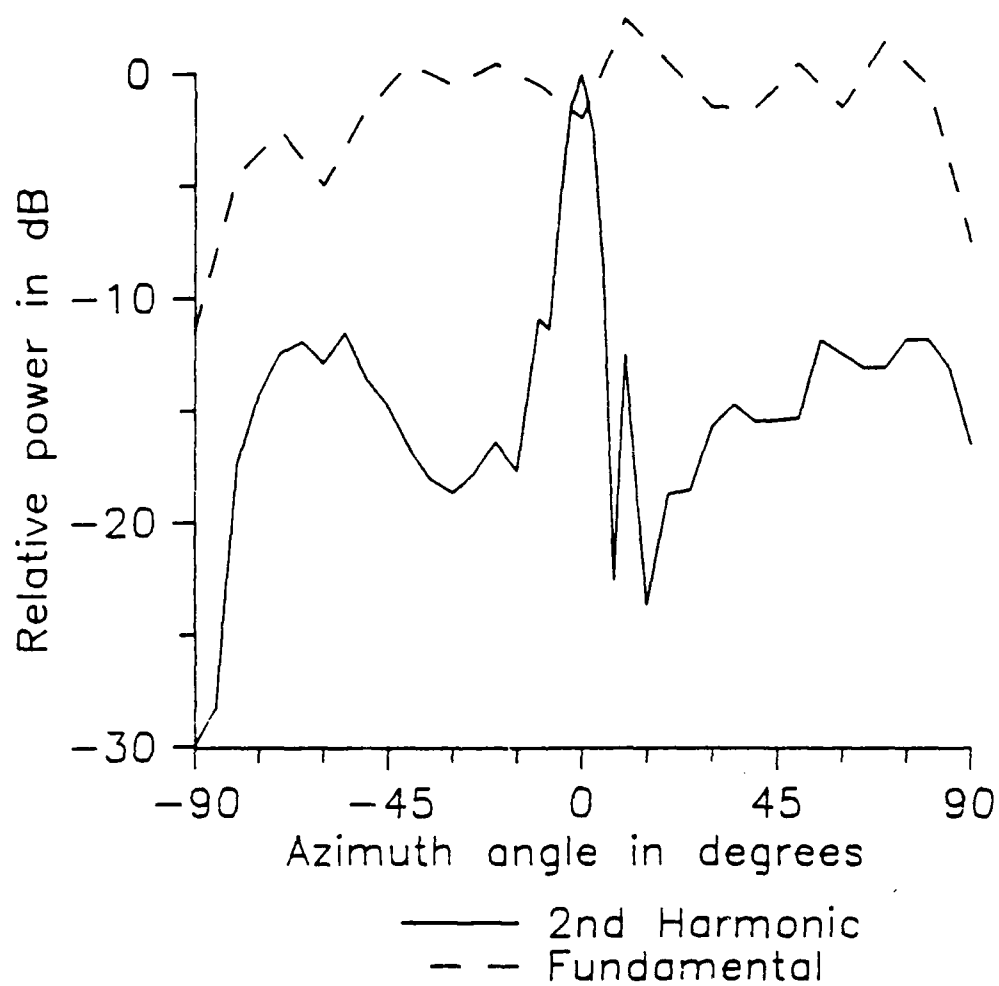
Figure 5.13 Calculated and measured H-plane patterns
for the push-pull oscillator.
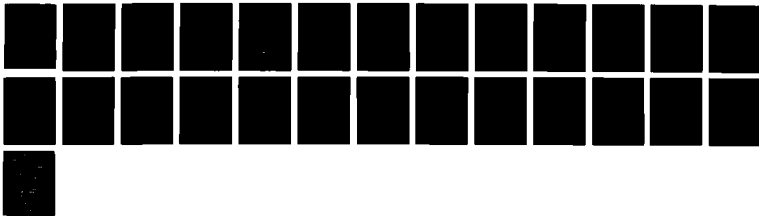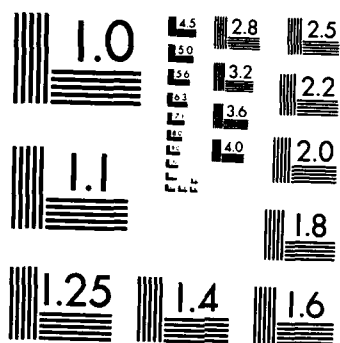
MICROCOPY RESOLUTION TEST CHART

NATIONAL BUREAU OF STANDARDS-1963-A
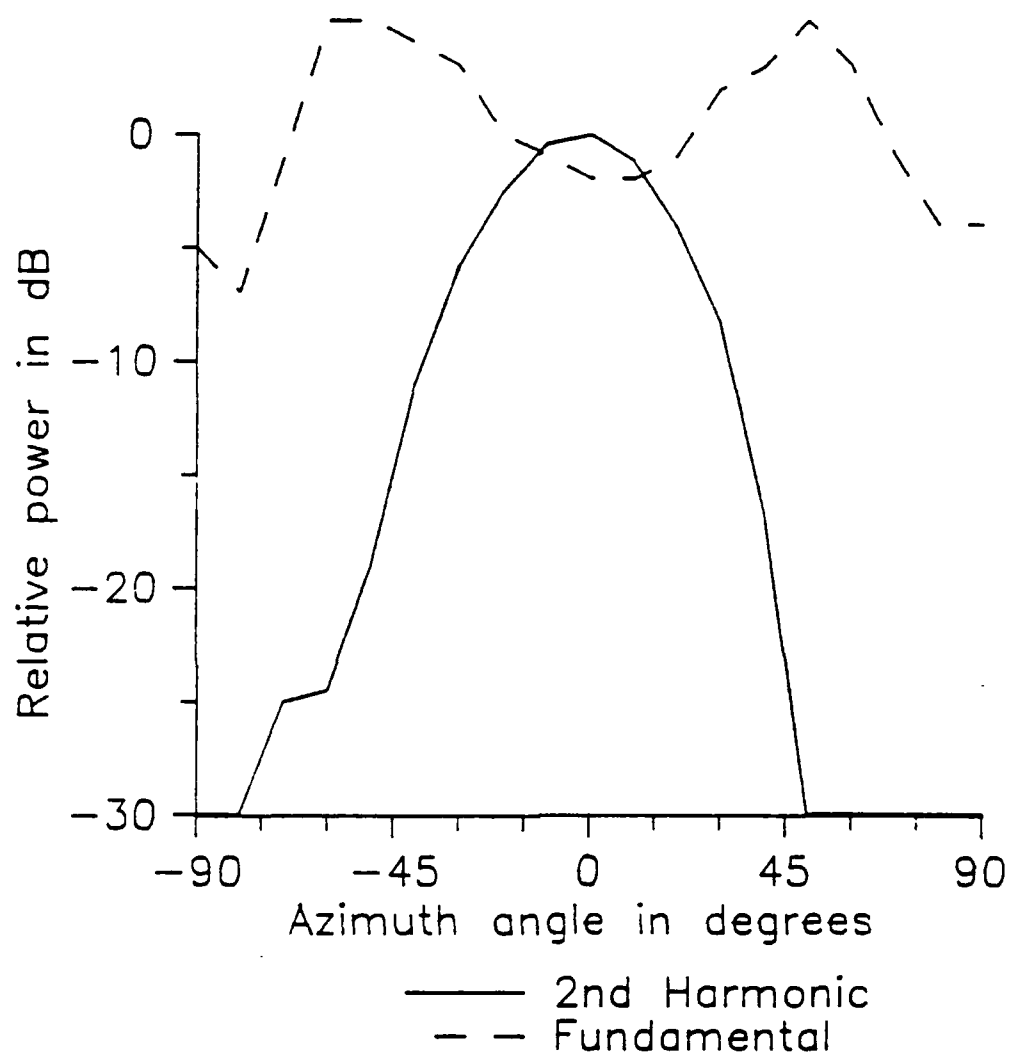
Figure 5.14 Calculated and measured H-plane patterns
for the push-pull oscillator.

CHAPTER 6: TRANSCEIVER CIRCUITS

The transceiver circuits described in this section operate in essentially the same fashion as the transmitter circuits described in the previous chapters, except the additional function of reception of microwave energy is incorporated. The received microwave energy incident on the antenna is channeled back to the oscillating FET (FETs) where these devices function as self-oscillating mixers for down-conversion of the received signal. The down-converted signals then are produced at frequencies of $mf_{received} \pm nf_{oscillator}$, and are extracted from the FET, in this case using an IF transformer. The circuit is therefore an extremely inexpensive microwave transceiver, which we will show later is acceptable for use as a Doppler motion detection module.

The idea of using self-oscillating mixers in Doppler radar is not new [35,36], although in the past diode oscillators were most often used. Tajima has reported the performance of FET self-oscillating mixers [37].and recently a novel application has been demonstrated [38]. To the author's knowledge, this dissertation is the first application of FET self oscillating mixers to microstrip-based transceiver circuits.

In the circuits described here, the received signal is injected into either the gate or the drain of the FET(s), and the IF signal is extracted at the drain using an IF transformer. The transformer is inserted in the drain bias line to pick off the IF signal without requiring a complicated bias tee arrangement. This approach limits the IF range to lower frequency ranges.

For efficient conversion of the received signal. it is desirable to operate the FET in a highly non-linear fashion. For the single device transceiver, it was convenient to bias the FET so that the operating current was near I_{DSS}. For the dual device

transceiver, the FETs were operated with an open circuit on the gate. In both cases it was found that the conversion gain was strongly dependent on the bias point.

The single device transceiver circuit appears in Figure 6.1. The circuit tested was a modified version of the oscillator circuit described in Chapter Four which had a seven element band-stop filter on the gate and a twelve element patch array antenna. The circuit was modified by attaching the IF transformer as shown in the figure. The transformer used was a Mini-Circuits™ TI-6T with 3dB cutoff points at 3 kHz and 300 MHz, and an impedance transformation ration of 1:1. Although the low output impedance of the FET would indicate that some impedance transformation should be necessary, this transformer gave the best results. This transformer was used for the purpose of beam pattern measurement only, for Doppler performance assessment, an audio frequency transformer was used.

The transmit and received patterns are shown in Figure 6.2. The primary importance of this figure is that it shows that the received power which is responsible for the IF signal is received by the antenna, and does not leak into the circuit from some other port, such as the gate of the device. These patterns were measured at an IF frequency of 6 MHz.

Similarly to the isotropic transmit gain, G_{iso}^T, defined in Chapter Four, we define here an isotropic receive gain, G_{iso}^R, as the ratio of IF power supplied by the transceiver to that of a hypothetical isotropic receiver with 100% RF-IF conversion efficiency. This parameter is determined in a fashion exactly similar to that described for G_{iso}^T shown in Figure 4.11. In Figure 6.3 we show the values of G_{iso}^R versus V_{DS} for three different values of IF frequency. The maximum value of 11.4 dB occurs at the point where the oscillation has just begun. The circuit exhibited strange behavior in this region, with the

IF out

Microstrip patch array

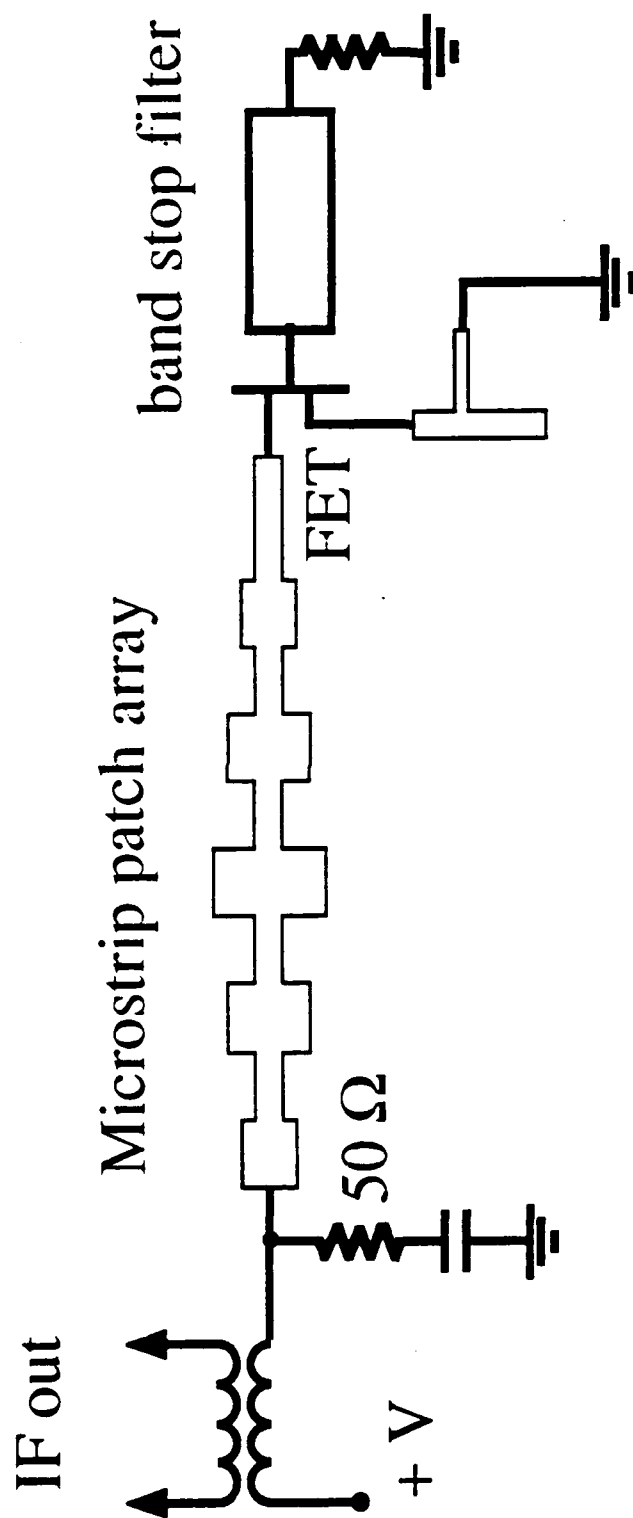band stop filter

50 Ω

FET

+ V

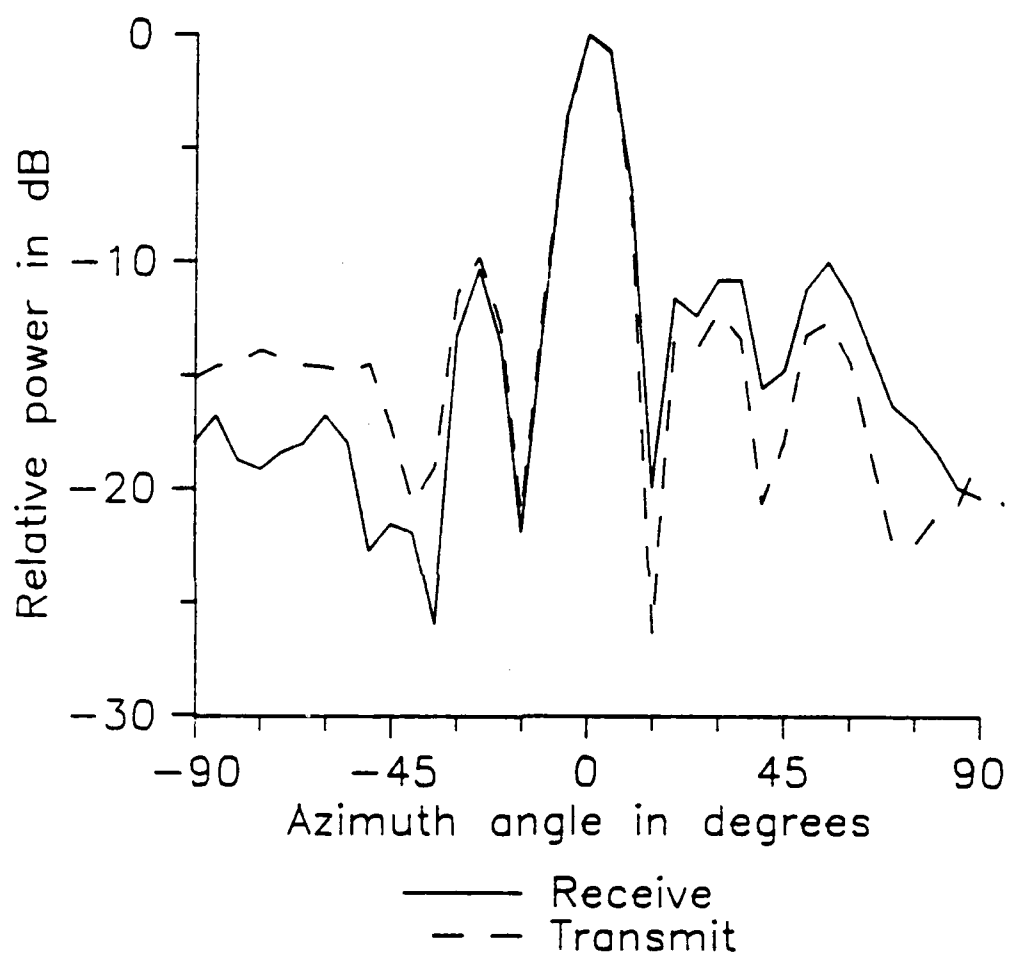Figure 6.1 The single device transceiver circuit.

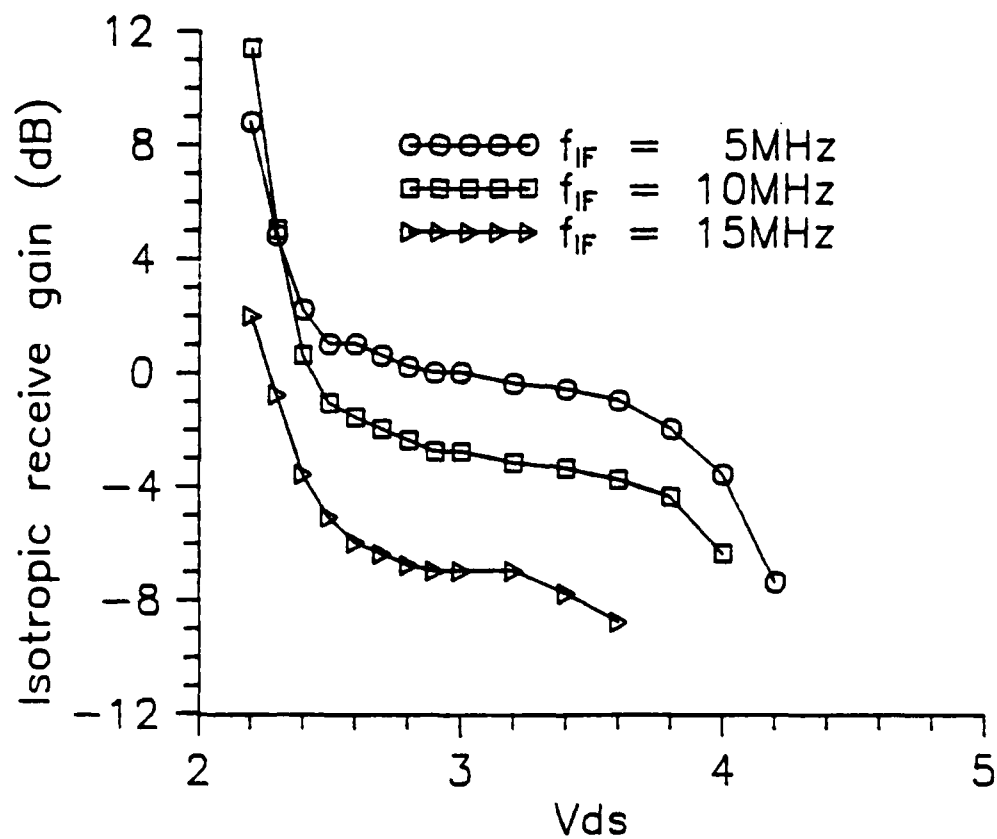Figure 6.2   E-plane transmit and receive patterns for the single device transceiver circuit.

Figure 6.3 G_{iso}^R vs. V_{DS} for the single device transceiver.

conversion gain varying quite rapidly with IF frequency at particular frequencies. It is believed that operation in this region is unstable, since the device is on the verge of oscillation. It is expected that more consistent performance will be obtained at more stable operating points.

The only readily available tuning mechanism for this circuit with this bias arrangement is variation of the drain voltage, since both the gate and source terminals are dc short circuited. This results in a narrower tuning range for the circuit, as shown in Figure 6.4. In Figure 6.5 the ERP and G_{iso}^T versus V_{DS} for the single device transceiver is shown.

The dual device transceiver circuit is shown schematically in Figure 6.6. The circuit is designed so that the FETs oscillate in the odd mode, as in the push-pull oscillator circuit. In this case, however, a separate antenna is added to the gates of the FETs for the purpose of receiving the incoming signal. As is the case for most dual device FET mixers [39], a hybrid circuit is required: in this case, a center-tapped IF transformer is used. Since the gate antenna appears at the virtual ground point in the circuit, it is well isolated from the transmitting oscillation. The gate antenna is also a rampart line structure, with the field polarized perpendicular to its axis. In this way, the transmitted and received fields are polarized in the same direction, which is desired for Doppler applications.

This transceiver is designed to operate in the following way: The FETs oscillate in the push-pull mode and generate the transmitted signal as described in Chapter five. The Doppler shifted signal returning from the target then is received by the gate antenna and is applied to the gates of the FETs in the even mode. Since the FETs are oscillating in the odd mode and the received signal is present in the even mode, the IF signal at
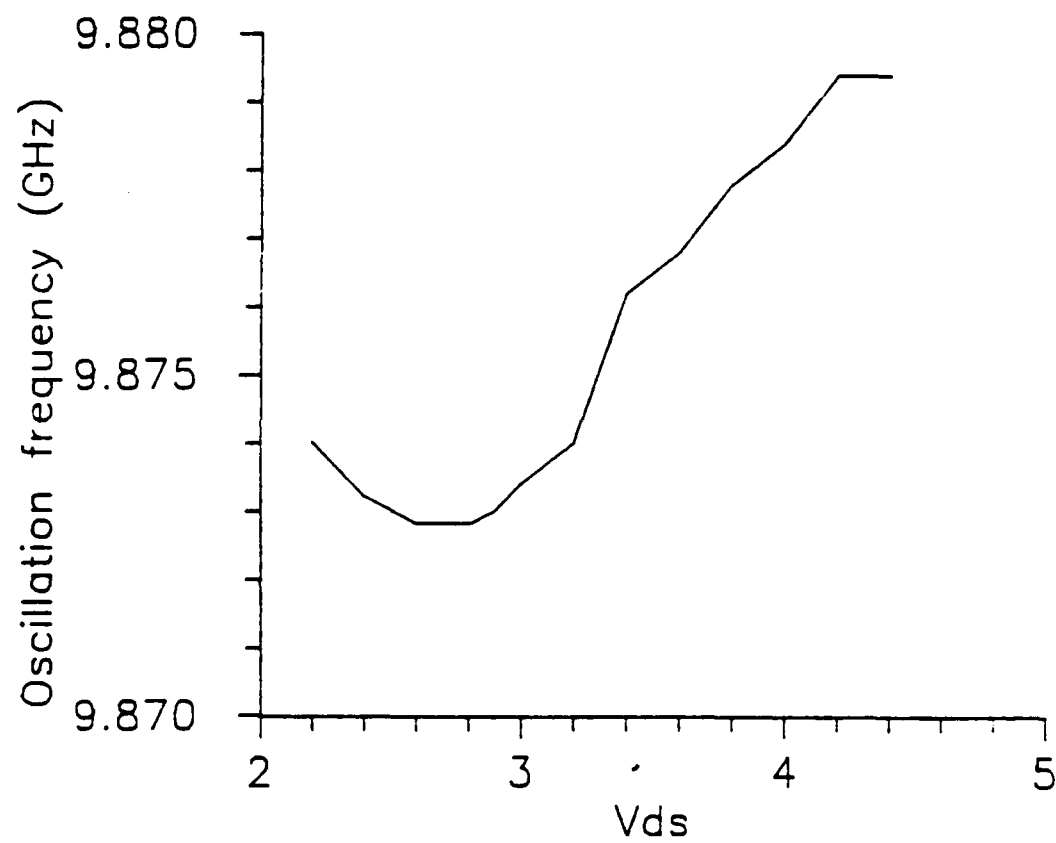
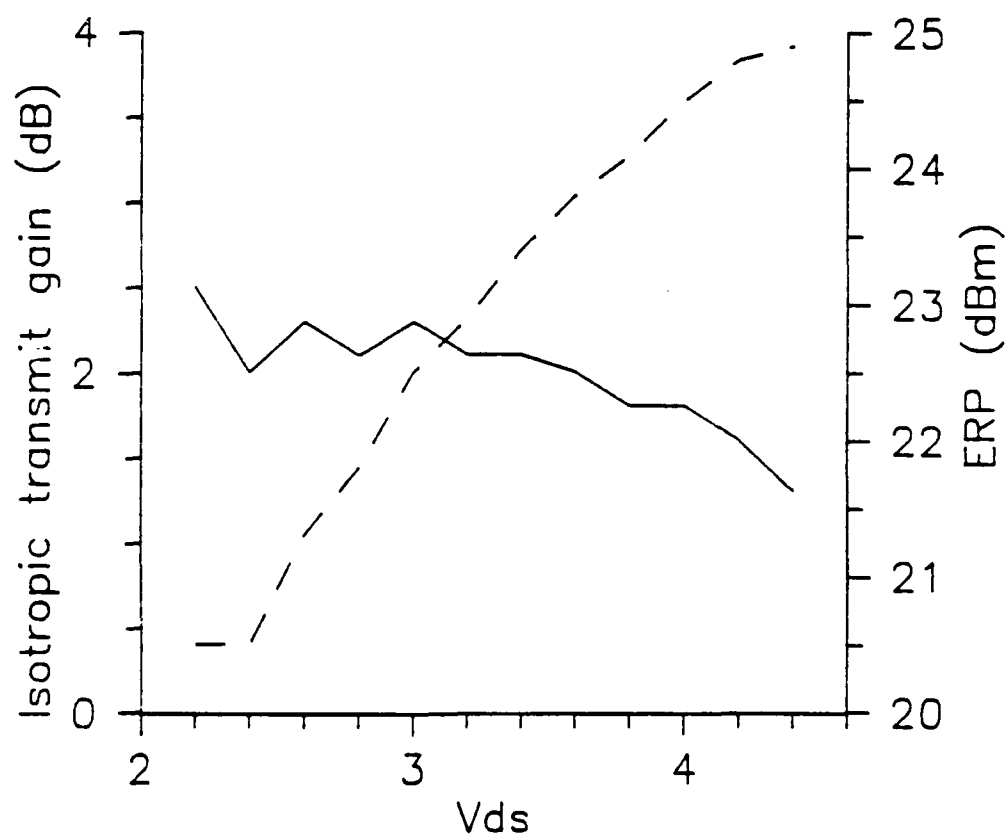Figure 6.4   Tuning range vs. V_{DS} for the single device transceiver.

Figure 6.5   ERP and G_{iso}^T vs. V_{DS} for the
single device transceiver.

transmit antenna
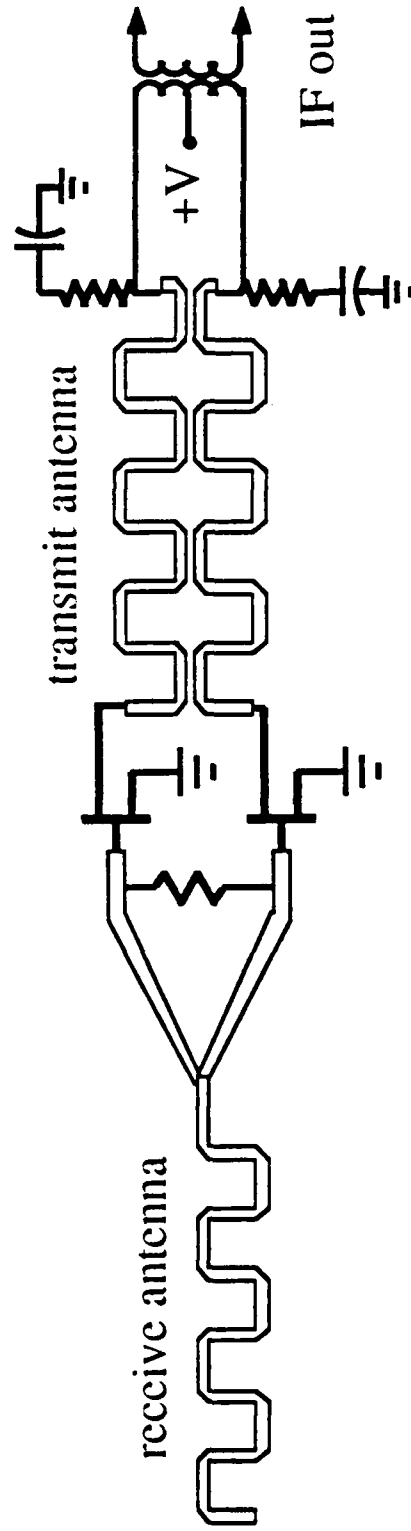
+V

IF out

receive antenna

Figure 6.6 Schematic view of the dual device transceiver circuit

$f_{IF} = f_{received} \pm f_{oscillator}$ will be generated in the odd mode. The IF signal then passes through the IF transformer in the odd mode, and the powers are combined in the secondary circuit. The bias signal is supplied through the center tap on the primary, which is on the axis of symmetry of the circuit. In this circuit, the FETs are biased with the gates open-circuited. This means that the device is operating very near pinch-off, which should insure a highly non-linear operation.

The dual device approach was tried for several reasons. First of all, with the separate receive antenna, it is possible to insert an RF preamplifier into the circuit between the antenna and the gate, and thereby improve the circuit performance greatly. The main advantage of this addition is that the noise figure of the transceiver would then be dominated by that of the preamplifier, which can be made very low using a FET or HEMT. Secondly, in a single FET circuit, it is difficult to attach an antenna directly to the gate of the FET. However, we expect that by stimulating the FET at the gate port, we may be able to increase the conversion gain of the FET mixer, since the gate capacitance is one of the major non-linearities in the FET.

The dual device circuit was fabricated on Rogers Duroid 5880 with a thickness of 0.51 mm as before. However, this time the additional length of the circuit due to the gate antenna required that the coupled rampart line antennas on the drain be held to only five sections, so that the overall length of the circuit would be under about 20 cm, which is the length below which circuits can be easily processed. Since the number of elements of the coupled rampart line antenna was reduced, the stop-band width would be increased for a given stop-band return loss. For the purpose of pattern measurement, a TI-6T IF transformer was again used.

Although the circuit was designed for operation at 10 GHz, the actual operation frequency turned out to be at 9.17 GHz. This was believed to be due to the fact that the shorter resonant element on the drain was less selective, thereby allowing the operation at a lower frequency. It is also possible that this behavior is due to poorly matched transistors.

The H-plane transmit and receive patterns are shown in Figure 6.7. It is immediately obvious that the transmit and receive patterns are skewed, and therefore the module is "cross-eyed". This is due to the module oscillating far from the design frequency. This is a problem, since for radar applications, we desire that the receive and transmit antennas point in the same direction.

The E-plane patterns are shown in Figure 6.8. In this plane also, we see that the beams are not pointing in the same direction. Once again this is due to the operation at a frequency off from the design point. Although these problems are not fundamental to the circuit design, and can be overcome by a redesign, they point out the disadvantages of a dual antenna system for transceiver modules.

In this circuit, the tuning was again accomplished by varying the drain voltage. Figure 6.9 shows the oscillation frequency and G_{iso}^{R} versus V_{DS} for the dual device oscillator circuit. Once again we see that the receive gain is a maximum at the lowest bias points, and decreases with increasing V_{DS}. Also, for this circuit, we notice an improvement in the tuning range to about 70 MHz. In Figure 6.10 the ERP and G_{iso}^{T} versus V_{DS} are shown. We note that the maximum ERP is the approximately equal for the single and dual device circuits, and that the maximum G_{iso}^{T} is 3 dB higher for the latter case. Of course, this is not an indication of power combining efficiency, since the devices are not biased at similar operating points.
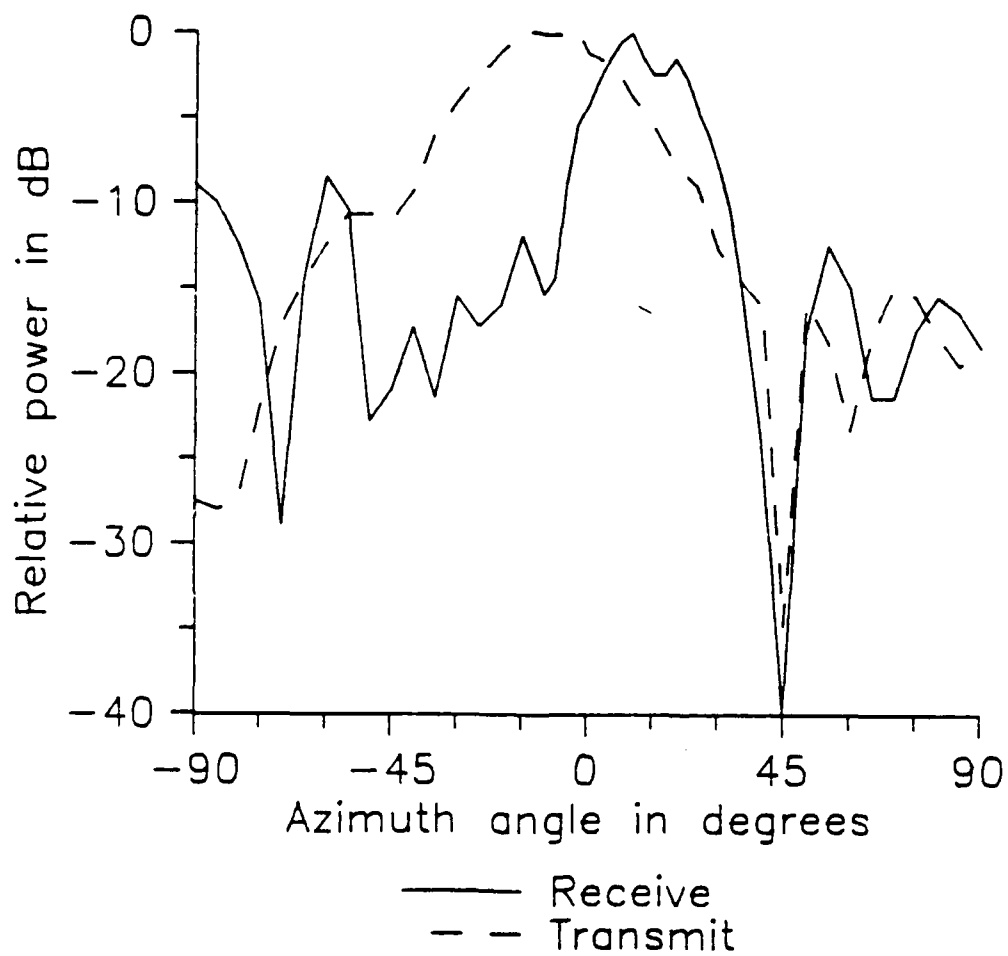
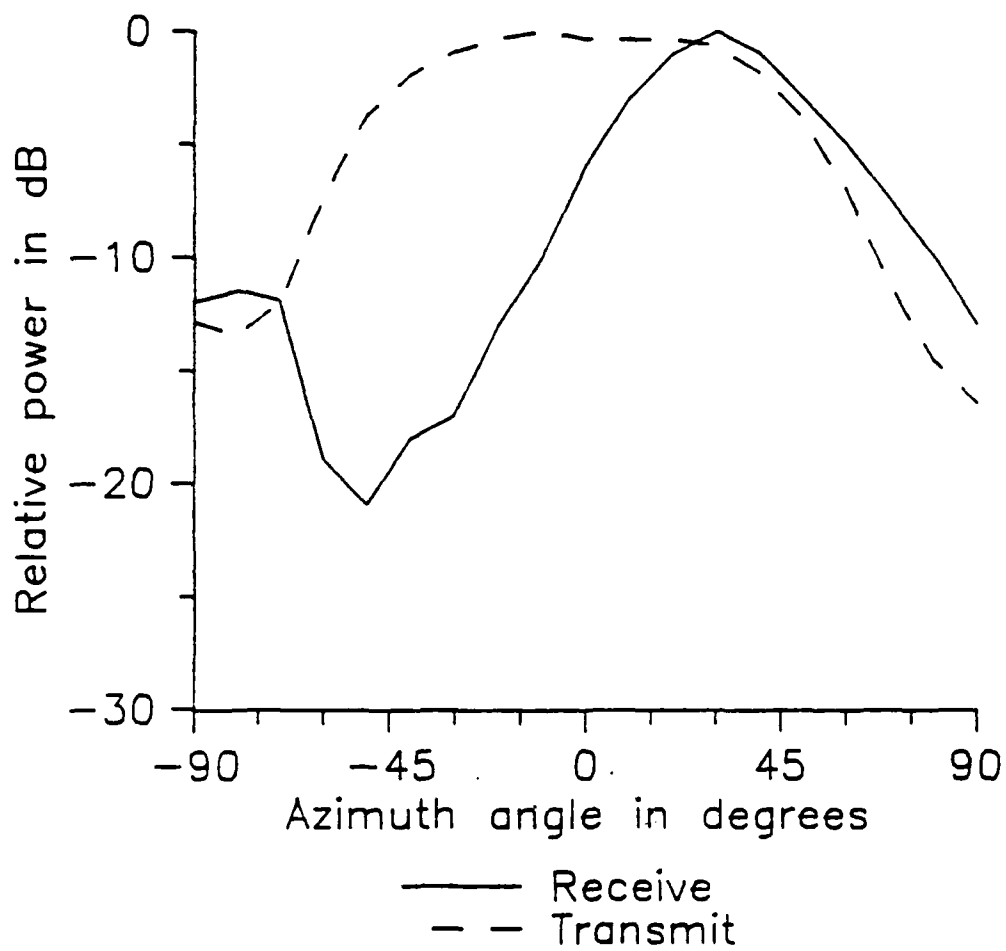Figure 6.7   H—plane transmit and receive patterns for the dual device transceiver circuit.

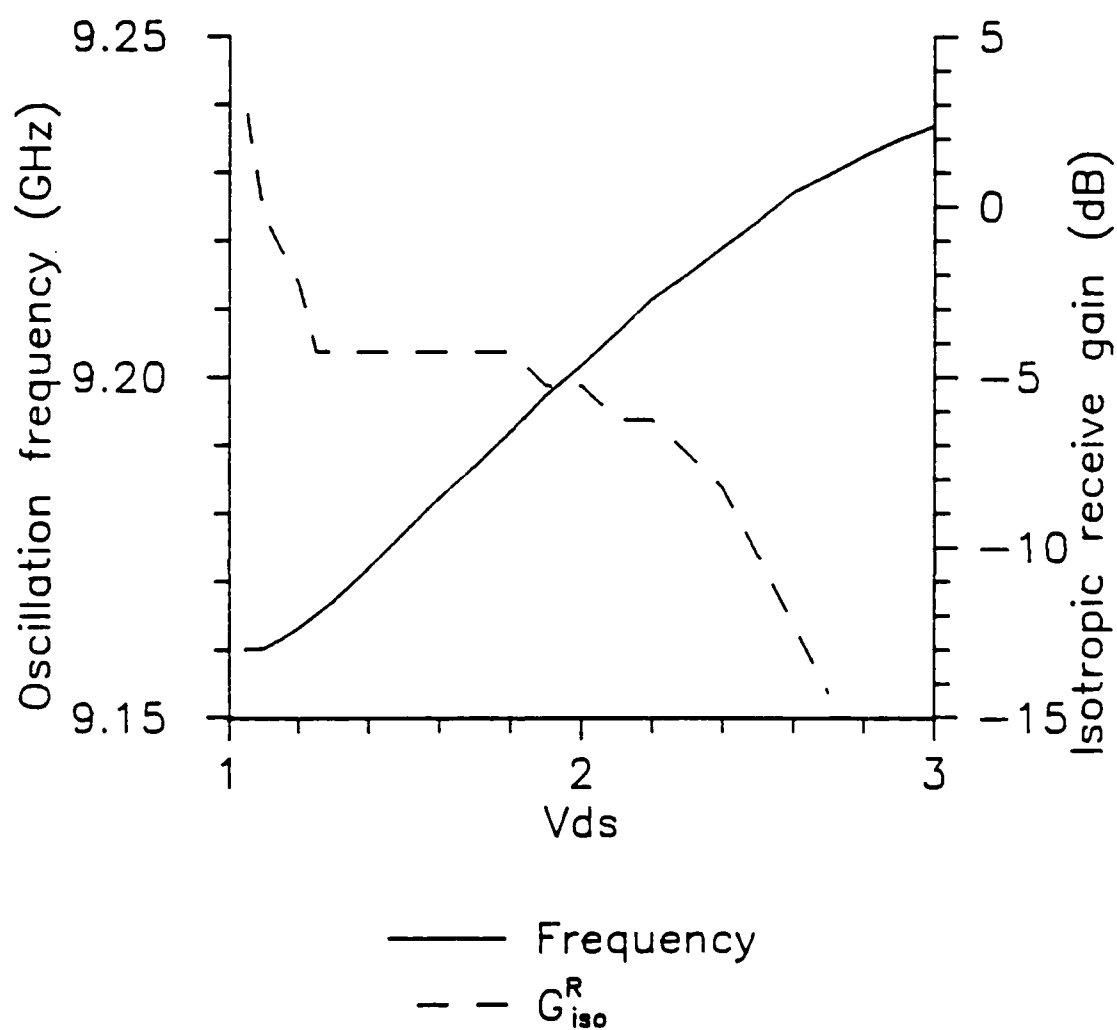Figure 6.8   E—plane transmit and receive patterns for the dual device transceiver circuit.

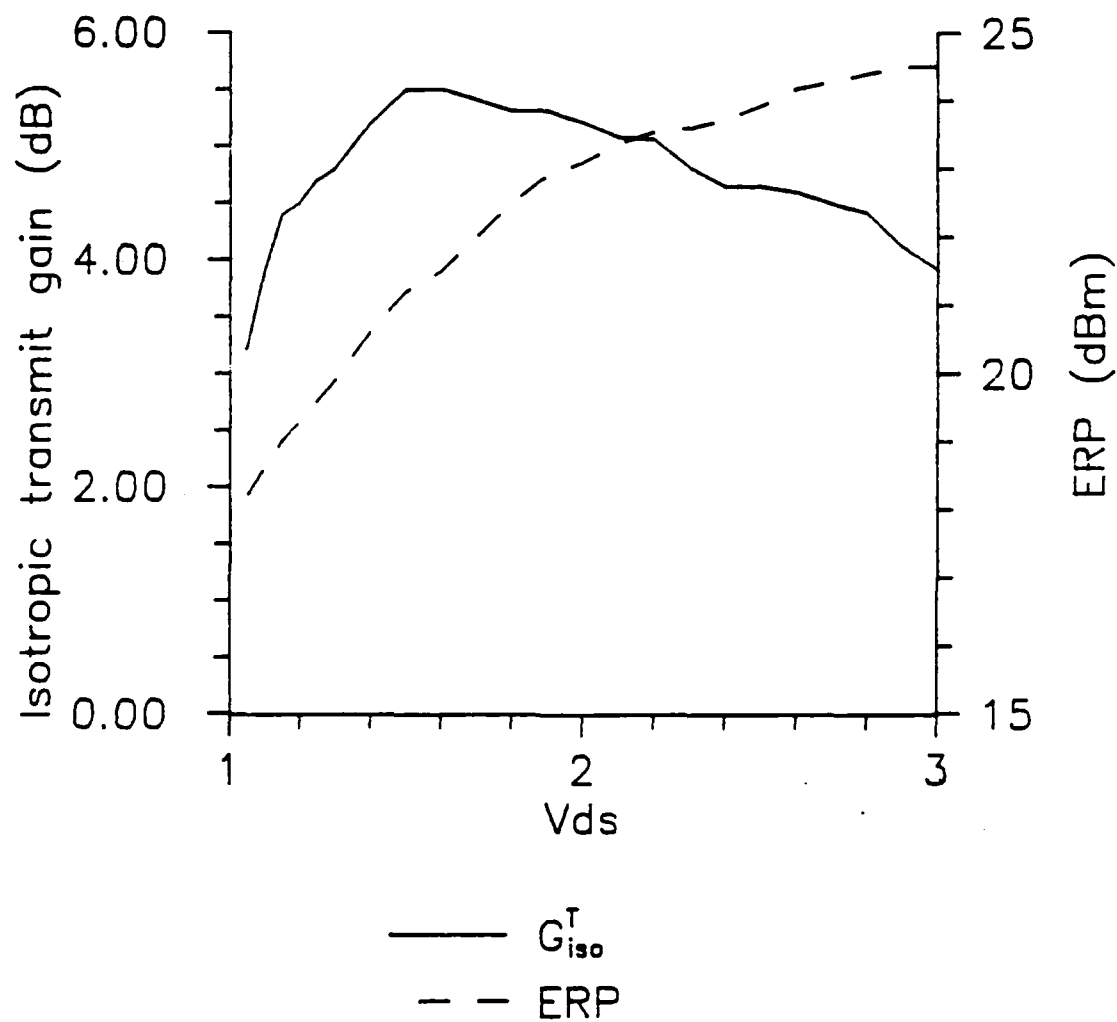Figure 6.9   Frequency and G^R_{iso} vs. V_{DS} for the dual device transceiver.

Figure 6.10 G^T_{iso} and ERP vs. V_{DS} for the dual device transceiver.

A summary of the performance of both transceiver modules is given in Table 6.1

It is appropriate at this point to determine if this circuit is appropriate for Doppler radar applications. We may divide these applications into two categories [36]: long range Doppler where $\omega_d \tau \geq 1$; and short range Doppler, where $\omega_d \tau \ll 1$. Here, ω_d is the Doppler shift frequency, $\omega_d = 2vf_0/c$, where v is the velocity of the target, f_0 is the oscillator frequency, and c is the velocity of light, and τ is the round trip transit time to the target. In long-range Doppler systems, coherence of the transmitted signal and power levels are of primary importance, the transceiver circuits described above are not appropriate in their present form. However, these same circuits may be appropriate for short-range applications such as motion detection and police radar.

We may estimate the range of the modules described above using the radar range equation [40]. We derive this equation by determining the range where the received IF power, P_{IF}, is equal to the minimum detectable signal.

The IF signal due to the reflection from the target is given by

$$P_{IF} = \frac{ERP}{4\pi R^2} \frac{\sigma}{4\pi R^2} \frac{\lambda^2 G_{iso}^R}{4\pi} , \qquad (6.1)$$

where R is the distance to the target and σ is the radar cross-section of the target. The term involving G_{iso}^R is the effective aperture of the receive antenna. To determine the minimum detectable signal, we use the noise figure of the circuit, given by

$$F_o = \frac{S_i/N_i}{S_o/N_o} \qquad (6.2)$$

	Maximum isotropic transmit gain		Maximum isotropic receive gain		Maximum ERP	
	Value	dc bias	Value	dc bias	Value	dc bias
Single device transceiver	2.5 dB	4.4 V	8.8 dB	2.2 V	24.9 dBm	4.4 V
Dual device transceiver	5.5 dB	1.6 V	2.7 dB	1.05 V	24.5 dBm	3.0 V

Table 6.1 Isotropic transmit and receive gain and ERP for transceiver circuits.

where S_i and N_i are the signal and noise levels at the input of the circuit, and S_o and N_o are the corresponding quantities at the output (IF). N_i is given by

$$N_i = kT_oB_n$$

where k is Boltzmann's constant, $1.38 - 10^{-21}$ W/Hz, T_o is 290 K, and B_n is the receiver bandwidth; $kT_o = -174$ dB/Hz. If we define the minimum detectable signal as being 3dB above the noise floor, then $S_{min} = N_o$ with no input signal present, or

$$S_{min} = F_oGkT_oB_n \tag{6.3}$$

where G is now the gain of the mixer alone. Since we do not have data for G and F_o at our disposal, we must use reasonable estimates for these values. Huang, et. al. [38] have measured 10 dB for F_o in similar FET self-oscillating mixer circuits; we will somewhat arbitrarily use a value of 10 dB conversion loss for G. Equating (6.3) to (6.1) gives:

$$R^4 = \frac{ERP \, \sigma \, \lambda^2 G_{iso}^R}{(4\pi)^3 F_oGkT_oB_n}$$

For Doppler applications such as motion detection and velocimetry, B_n need not be more than 5 kHz. If we substitute typical values taken from the above measured data for the single device oscillator at $V_{DS} = 2.6$ V, the resulting value for the range is about 20 m. This is about the operating range for motion detection modules.

The other primary concern is the FM noise of the oscillator. This problem is discussed in [36]. The conclusion from their discussion is that the FM noise limits the range of self-oscillating mixers to distances of c/f, where f is a frequency from the carrier above which the FM noise becomes negligible. In the case of our short range application, this f should be of the order of 10 MHz. Although precise noise skirt measurements are difficult to perform using the spectrum analyzer, observation of the oscillator spectrum indicates that this requirement is not a problem.

To test the performance of the modules as Doppler motion detection devices, the RF transformer was replaced with an audio transformer, and its output was connected to the input of an oscilloscope. No IF filtering was used. With this arrangement, the motion of objects in front of the circuits could be measured. The most sensitive circuit was that using the single device. With this setup, the motion of a man walking slowly approximately 4 m in front of the circuit could be measured. Frequencies as low as 3 Hz were observed on the oscilloscope, and IF voltages as high as 1 V peak to peak were measured. The dual device transceiver did not perform as well, most likely due to the problems of the antennas looking in different directions.

It is difficult to obtain quantitative data on Doppler modules without elaborate test setups. However, the above results indicate that the transceiver modules are appropriate for motion detection systems. With additional IF filtering and frequency counting circuitry they should be applicable to velocimetry.

CHAPTER 7: CONCLUSIONS

In this dissertation we have presented the design and test of two types of planar oscillator modules for the generation of microwave power. We have also presented the resulting transceiver modules which can be constructed from these circuits with the addition of receiving elements. The circuits are very simple and inexpensive, can be fabricated quickly and require little alignment.

The prototype circuits were constructed at x-band to minimize test and fabrication time, however, the same approach may be applied at shorter wavelengths. FET oscillators are capable of operation into the millimeter-wave range, and antennas of the same construction as those described here have been reported in operation at frequencies up to 70 GHz [26]. It is reasonable to expect that these circuits may be employed as a components in quasi-optical power combining schemes [2]. This is the expected use for the push-push oscillator. It has also been mentioned recently that surface-emitting oscillators such as those described here have applications in ECM [10].

The transceiver circuits are ideally suited for short-range Doppler motion detection applications. Compared to conventional Doppler modules, which consist usually of Gunn diodes and waveguide hardware, they are smaller, lighter, consume less power, and are likely to be less expensive to manufacture.. The microstrip construction also permits a degree of conformability in the mounting. With little modification these transceivers could be applied to such non-critical motion detection applications as door-openers, etc. With some additional IF filtering they may have applications in velocimetry.

BIBLIOGRAPHY

[1]   *Microwave Sensing Modules and Sources*, Publication Number 50050200, Alpha Industries, Inc., Semiconductor Division, Woburn, MA, 1987.

[2]   J.W. Mink, "Quasi-optical power combining of solid-state millimeter-wave sources," *IEEE Trans. Microwave Theory Tech.*, vol MTT-34, pp. 273-279, 1986.

[3]   C.M. Jackson. J.A. Lester, M.A. Yu, and Y.C. Ngan, "Quasi-optical patch mixers at 35 and 94 GHz," in *1988 IEEE MTT-S Int. Microwave Symp. Dig.* (New York), pp. 781-784, 1988.

[4]   V.D. Hwang, T. Uwano, and T. Itoh, "Quasi-optical integrated antenna and receiver front end," *IEEE Trans. Microwave Theory Tech.*, vol MTT-36, pp. 80-85, 1988.

[5]   K.D. Stephan and T. Itoh, "A planar quasi-optical subharmonically pumped mixer characterizedby isotropic conversion loss," *IEEE Trans. Microwave Theory Tech.*, vol. MTT-32. pp. 97-102, 1984.

[6]   S. Nam, T. Uwano and T. Itoh, "Microstrip-Fed Planar Frequency-Multiplying Space Combiner," *IEEE Trans. Microwave Theory Tech.*, vol MTT-35, pp. 1271-1276, 1987.

[7]   N. Camilleri and B. Bayraktaroglu, "Monolithic millimeter wave IMPATT oscillator and active antenna," in *1988 IEEE MTT-S Int. Microwave Symp. Dig.* (New York), pp. 955-958, May 1988.

[8]   K.A. Hummer and K. Chang, "Microstrip active antennas and arrays," in *1988 IEEE MTT-S Int. Microwave Symp. Dig.* (New York), pp. 955-958. May 1988.

[9]   K.D. Stephan, "Inter-injection-locked oscillators for power combining and phased arrays," *IEEE Trans. Microwave Theory Tech.*, vol.MTT-34. pp. 1017-1025, 1986.

[10]   Z.B. Popovic, M. Kim and D.B. Rutledge, "Grid oscillators," *Int. J. of Infrared and Millimeter-Waves*, vol. 9, pp. 647-654, 1988.

[11]   P.D. Batelaan, M.A. Frerking, T.B.H. Kuiper, H.M. Pickett, M.M. Schaefer. P. Zimmerman, and N.C. Luhman, Jr., "A dual-frequency 183/380 GHz receiver for airborne applications," *IEEE Trans. Microwave Theory Tech.*, vol.MTT-36, pp. 694-700, 1988.

[12]   B.-S. Song and T. Itoh, "Distributed bragg reflection dielectric waveguide oscillators," *IEEE Trans. Microwave Theory Tech.*, vol MTT-27, pp. 1019-1022, 1979.

[13]   R.E. Collin and F.J. Zucker, *Antenna Theory*. New York: Wiley, 1969, pt II, ch 19.

[14]   P.J. Crepeau and P.R. McIsaac, "Consequences of symmetry in periodic structures," *Proc. IEEE,* vol 52, pp 33-43, 1964.

[15]   K. Kurokawa, "Some basic characteristics of broadband negative resistance oscillator circuits," *Bell Syst. Tech. J.*, vol.48, pp. 1937-1955, 1969.

[16]   K. Kurokawa, *An Introduction to the Theory of Microwave Circuits*. New York: Academic Press, 1969, ch. 9.

[17]   T. Bercelli, *Nonlinear Active Microwave Circuits*. Amsterdam:Elsevier, 1987, ch. 2.

[18]   G. Gonzalez, *Microwave Transistor Amplifiers; Design and Analysis*. Englewood Cliffs, N.J.: Prentice-Hall, 1984, ch. 7.

[19]   G.D. Vendelin, *Design of Amplifiers and Oscillators by the S-Parameter Method*. New York: Wiley, 1982, ch. 1.

[20]   Y.T. Lo, D. Soloman, and W.F. Richards, "Theory and experiment on microstrip antennas," *IEEE Trans. Antennas Propagat.*, vol. AP-27, pp. 137-145, 1979.

[21]   I.J. Bahl and P. Bhartia, *Microstrip Antennas*. Dedham, Mass.: Artech House, 1980.

[22]   J.R. James and A. Henderson, "High frequency behavior of microstrip open-circuit-terminations," *IEE J. Microwaves, Optics and Acoustics*, vol. 3, pp. 205-218, 1979.

[23]   K.C. Gupta, R. Garg, and I.J. Bahl, *Microstrip Lines and Slotlines*. Dedham, Mass.: Artech House, 1979.

[24]   R.K. Hoffman, *Handbook of Microwave Integrated Circuits*. Dedham, Mass.: Artech House, 1988.

[25]   R. Sorrentino and S. Pileri, "Method of analysis of planar networks including radiation loss" *IEEE Trans. Microwave Theory Tech.*, vol. MTT-29, pp. 942-948, 1981.

[26]   J.R. James, P.S.Hall, and C. Wood, *Microstrip Antenna Theory and Design*. Stevenage, UK: Peregrinus, 1981.

[27]   L. Lewin, "Spurious radiation from microstrip," *Proc. IEE*, vol. 125, pp. 633-642, 1978.

[28]   I.J. Bahl, "Build microstrip antennas with paper-thin dimensions,"
        Microwaves, vol. 18, pp. 50-63, 1979.

[29]   P.S. Hall, "Microstrip linear array with polarization control," *IEE Proc.*, vol.
        130, part H, no. 3, April 1983.

[30]   T.G. Bryant and J.A. Weiss, "Parameters of microstrip transmission lines and
        of coupled pairs of microstrip lines," *IEEE Trans. Microwave Theory Tech.*,
        vol. MTT-16, pp. 1021-1027, 1968.

[31]   T. Itoh, "Spectral domain immitance approach for dispersion characteristics of
        generalized printed transmission lines," *IEEE Trans. Microwave Theory Tech.*,
        vol. MTT-28, pp. 733-736, 1980.

[32]   M. Kirschning and R. Jansen, "Accurate wide-range design equations for the
        frequency-dependent characteristics of parallel-coupled microstrip lines," *IEEE
        Trans. Microwave Theory Tech.*, vol. MTT-32, pp. 83-90, 1984.

[33]   D.C. Park, G.L. Matthaei, and M.S. Wei, "Bandstop filter design using a
        dielectric waveguide rating," *IEEE Trans. Microwave Theory Tech.*, vol. MTT-
        32, pp. 83-90, 1984.

[34]   J.R. Bender and C. Wong, "Push-push design extends bipolar frequency
        range," *Microwaves and RF*, vol. 22, pp. 91-98, 1983.

[35]   S. Nagano, H. Ueno, H. Kondo, and H. Murakami, "Self-excited microwave mixer with a Gunn diode and its applications to Doppler radar," *Electron. Commun. Japan*, vol. 52, pp.112-114, 1969.

[36]   M.-S. Gupta, R.J. Lomax, and G.I. Haddad, "Noise considerations in self-mixing IMPATT diode oscillators short-range Doppler radar applications," *IEEE Trans. Microwave Theory Tech.*, vol. MTT-22, pp. 37-43, 1974.

[37]   Y. Tajima, "GaAs- FET applications for injection-locked oscillators and self-oscillating mixers," *IEEE Trans. Microwave Theory Tech.*, vol. MTT-27, pp. 629-632, 1979.

[38]   V.D. Hwang, T. Uwano, and T. Itoh, "Quasi-optical integrated antenna and receiver front end." *IEEE Trans. Microwave Theory Tech.*, vol MTT-36. pp. 80-85, 1988.

[39]   S.A. Maas, *Nonlinear Microwave Circuits*. Dedham.Mass.: Artech House, 1987.

[40]   M.I. Skolnik, *Introduction to Radar Systems*. New York: McGraw-Hill, 1980.